Advancing Drought Monitoring and Prediction Using a Multi-Index Multivariate Framework

(Award No. NA14OAR4310222)

Lead PI: Amir AghaKouchak
University of California, Irvine
Engineering Gateway, Irvine, CA 92697
Phone: 949-824-9350, Email: amir.a@uci.edu

PI: Mark Svoboda
National Drought Mitigation Center
University of Nebraska-Lincoln
3310 Holdrege Street,
Lincoln, NE 68583
Phone: 402-472-8238, Email: msvoboda2@unl.edu

PI: Andy Wood
Research Applications Laboratory
National Center for Atmospheric Research,
3090 Center Green Dr. Boulder, CO 80301
Email: andywood@ucar.edu

Final Report - 2018

Advancing Drought Monitoring and Prediction Using a Multi-Index Multivariate Framework

Overview

This project addressed the two primary objectives of the MAPP-Drought program: (a) improving methodologies for global to regional-scale analysis and predictions and (b) developing integrated assessment and prediction capabilities relevant to decision makers, and particularly the opportunity to integrate diverse data sources. During the project period, our team has focused on different activities including:

- **(I)** Assessing the role of temperature during the 2011-2016 California drought;
- **(II)** Expanding, testing and implementing a multivariate drought analysis framework for combining multiple drought indicators probabilistically to improve drought monitoring and prediction;
- **(III)** Improving seasonal drought prediction by combining statistical and dynamical models.
- **(IV)** Amplified warming of droughts in the historical record and climate model projections
- **(V)** Understanding the impacts of future climatic warming on snow water equivalent and water availability in Sierra Nevada.

In the following, we have summarized the results and outcomes of the project.

(I) Assessing the role of temperature during the 2011-2016 California drought

Global warming and the associated rise in extreme temperatures substantially increase the chance of concurrent droughts and heatwaves. The 2014 California drought is an archetype of an event characterized by not only low precipitation but also extreme high temperatures. From the raging wildfires, to record low storage levels and snowpack conditions, the impacts of this event can be felt throughout California. Wintertime water shortages worry decision-makers the most because it is the season to build up water supplies for the rest of the year. In this study, we show that the traditional univariate risk assessment methods based on precipitation condition may substantially underestimate the risk of extreme events such as the 2014 California drought because of ignoring the effects of temperature. We argue that a multivariate viewpoint is necessary for assessing risk of extreme events, especially in a warming climate. This study discusses a methodology for assessing the risk of concurrent extremes such as droughts and extreme temperatures.

Considering precipitation deficit alone, the 2014 California drought is not the most extreme event in the historical record, with 243.6 mm average precipitation (red bar in Figure 1a). However, substantially warmer temperatures and several heatwaves during the 2014 California drought make this event unique and extreme. Over the past 119 years, November to April 2014 has been the warmest period on record (Figure 1b). In addition to extreme monthly temperature, several daily maximum temperature records were set across California. Figure 1c displays percent increase in maximum daily temperature relative to the mean daily maximum temperature

during January 13 to 20, 2014 when an extreme heatwave affected almost the entire state. The extreme daily maximum temperatures exceeded the mean by 90% in some locations, which led to very dry soil and significant stress on the ecosystem. If we consider only precipitation information, the return period (recurrence interval) of the 2014 California drought (November-April) is approximately 24 years. If we consider only temperature, the recurrence interval of the extreme heat during the California drought is estimated at approximately 120 years (see AghaKouchak et al., 2014 for details). Of course, extreme precipitation and temperature do not necessarily happen at the same time (e.g., 1977 with record precipitation extreme and near average temperature). However, an extreme condition combined with another non-extreme condition could lead to a compound extreme event with significant impacts.

An important question is: what is the risk of a compound extreme such as the 2014 California drought? We argue that in a changing climate, assessing the risk of climatic extremes (i.e., probability of occurrence of extremes) should be evaluated using a multivariate framework that can account for compound and concurrent extremes. Using the survival copula methodology presented in AghaKouchak et al. (2014), the combination of extreme precipitation and temperature conditions observed in 2014 in California appears to be a 200-year extreme event (Figure 1d). The blue dots in Figure 1d indicate historical observations of precipitation and temperature anomalies and the contour lines represent compound return periods from T=10 to T=200 years. An event in the upper right corner (lower left) in Figure 1d corresponds to a warm-dry (cold-wet) condition. Commonly used univariate risk estimation approaches significantly underestimate or overestimate the return period (risk of occurrence) of the 2014 California drought. Figure 1e indicates that the most extreme event (with respect to precipitation in California) had a recurrence interval of 120 years (the 1977 drought). However, with respect to both temperature and precipitation, the 1977 condition was only a 50-year event. On the contrary, the 2014 drought, even with more precipitation, is categorized as a more extreme event (200-yr return period) due to extreme temperature conditions. Figure 1e displays the compound extreme return levels of three extreme droughts in California (i.e., 1924, 1977, 2014) and their corresponding univariate precipitation-based return periods (x-axis in Figure 1). Our analysis demonstrates the importance of considering concurrent extremes, especially in light of the recent decades' rising temperatures. A compound extreme return period analysis approach allows obtaining more realistic estimates of risk of climate extremes. Noted, however, that for different hazards associated with different societal impacts, such compound risk estimation will depend on different combinations of univariate risk. In this case, for drought, impacts are tied not only to precipitation deficits but also water (and evaporative) demand, which is linked to temperature – thus the combination of these two variables is appropriate.

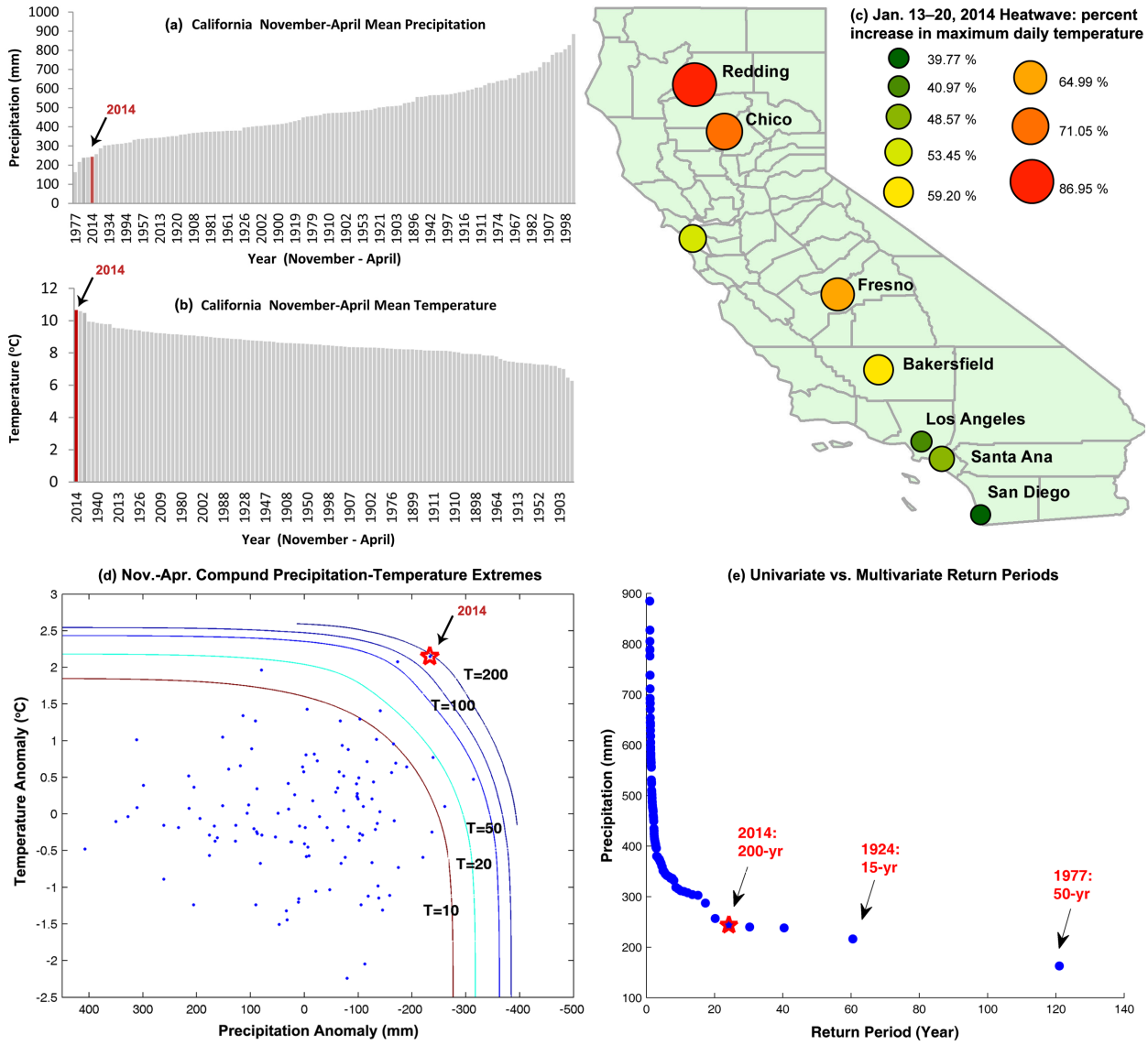

Figure 1: Ranked historical average precipitation (a) and temperature data for California. Percent increase in maximum daily temperature relative to the mean daily maximum temperature during January 13-20, 2014 (c). Compound temperature and precipitation extremes return period (d). Univariate empirical return period of extreme droughts in California and their corresponding compound extreme (red text) return periods (e).

(II) Expand, test and implement a multivariate drought analysis framework for combining multiple drought indicators probabilistically to improve drought monitoring and prediction

Numerous dynamic and statistical drought prediction models have been used for providing drought information and/or early warning. The concept of Ensemble Streamflow Prediction (ESP) has been used as a basis for forecasting such univariate drought indicators such as the widely-used Standardized Precipitation Index (SPI) for seasonal drought prediction.

In this study, we outline a framework for using the ESP concept for multivariate, multi-index drought prediction. We employ the recently developed Multivariate Standardized Drought Index (MSDI), which integrates precipitation and soil moisture for describing drought. In this approach, the ESP concept is first used to predict the seasonal changes to precipitation and soil moisture. Then, the MSDI is estimated based on the joint probability of the predicted accumulated precipitation and soil moisture as composite (multi-index) drought information. Given its probabilistic nature, the MSDI model offers both a measure of drought severity and probability of drought occurrence. This framework has been applied to soil moisture and precipitation individually and combined precipitation-soil moisture using MSDI, and was tested over the United States and East Africa (AghaKouchak 2014a; 2014b). The drought forecasting framework provides the probability occurrence of drought based on climatology and near-past observations of soil moisture. Our results indicate that soil moisture exhibits higher persistence than precipitation, and hence improves drought predictability (see Figure 2) in cases where precipitation occurs but is insufficient to overcome accumulated water deficits. Finally, the results indicate that the suggested multi-index predictions are consistent with the observation.

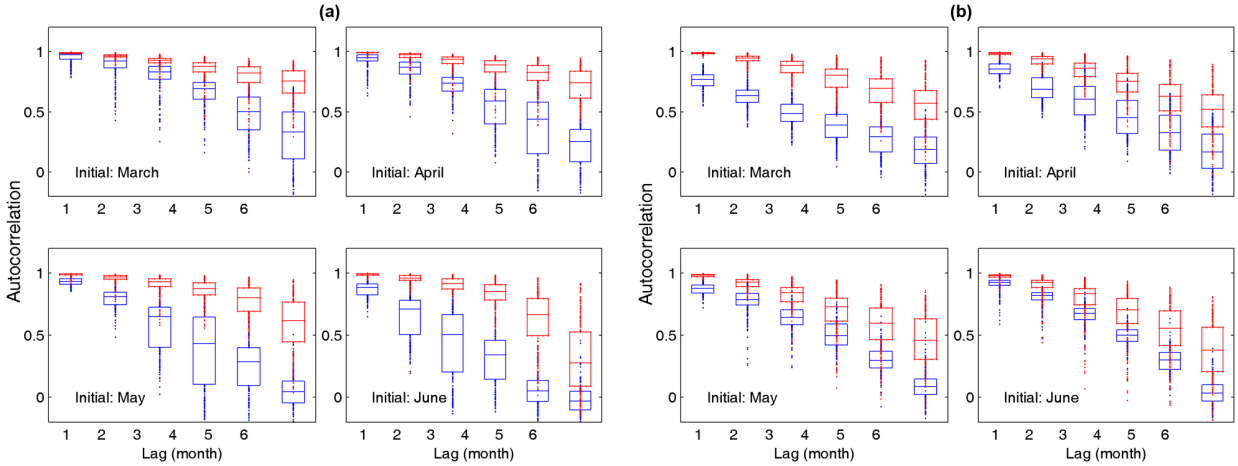

Figure 2 - Boxplots of autocorrelation coefficients (up to 6 months) of accumulated 6-month precipitation (blue) and soil moisture (red) from MERRA-Land for different initial month for (a) California and (b) Texas. The box plots show the median (center), 25th (lower) and 75th (upper) percentile edges.

(III) Improving seasonal drought prediction by combining statistical and dynamical models.

Improving water management in water stressed-regions requires reliable seasonal precipitation predication, which remains a grand challenge. Numerous statistical and dynamical model simulations have been developed for predicting precipitation. However, both types of models offer limited seasonal predictability. This study outlines a hybrid statistical-dynamical modeling framework for predicting seasonal precipitation. The dynamical component relies on the physically based North American Multi-Model Ensemble (NMME) model simulations (99 ensemble members). The statistical component relies on a multivariate Bayesian-based model

that relates precipitation to atmosphere-ocean teleconnections (also known as an analog-year statistical model). Here, the Pacific Decadal Oscillation (PDO), Multivariate ENSO Index (MEI), and Atlantic Multi-decadal Oscillation (AMO) are used in the statistical component. The dynamical and statistical predictions are linked using the so-called Expert Advice algorithm, which offers an ensemble response (as an alternative to the ensemble mean). The latter part leads to the best precipitation prediction based on contributing statistical and dynamical ensembles. It combines the strength of physically based dynamical simulations and the capability of an analog-year model. An application of the framework in the southwestern United States, which has suffered from major droughts over the past decade, improves seasonal precipitation predictions (3- to 5-month lead time) by 5-60 percent relative to the NMME simulations. Overall, the hybrid framework performs better in predicting negative precipitation anomalies (10-60% improvement over NMME) than positive precipitation anomalies (5-25% improvement over NMME). The results indicate that the framework would likely improve our ability to predict droughts such as the 2012-2014 event in the western United States that resulted in significant socio-economic impacts.

Introduction

Water supply reliability is a major challenge in the southwestern United States (US), with its growing population and industry. The region has experienced several droughts in the past (Seager et al., 2005; Woodhouse et al., 2010; Shukla et al., 2015; Cheng et al., 2016) and is likely to experience more frequent and severe droughts in the future (Seager et al., 2007; Cayan et al., 2010; Cook et al., 2015). The water supply in some parts of the region (e.g. California and Nevada) relies on winter precipitation, when most of the annual rainfall occurs (Cayan et al., 1998). The ongoing 2012-2015 California drought has led to more than a year's worth of precipitation deficit (Savtchenko et al., 2015). The rainy seasons in 2014 and 2015 were also the warmest two years in the past 120 years (Shukla et al., 2015; AghaKouchak et al., 2014). Such combinations of below normal precipitation and high temperature can significantly exacerbate the impacts of drought by promoting wildfires (Westerling et al., 2003; Keeley et al., 2009) and reducing snowpack in high elevations (Shukla et al., 2015).

The sustainable management of water resources in a region with frequent droughts requires timely and reliable seasonal precipitation forecasts. A community report on California drought issues that was developed based on inputs from decision-makers and stakeholders identified seasonal drought prediction as the key challenge facing the research community (AghaKouchak et al., 2015). The observed relationship between precipitation and the ocean-atmosphere teleconnections (Ropelewski and Halpert, 1986; Bradley et al., 1987; McCabe and Dettinger, 1999) has inspired the investigation and use of statistical analog-year models for seasonal precipitation forecasting (e.g., Hartmann et al., 2008; Wu et al., 2009; Schepen et al., 2012; Peng et al., 2014). Many alternatives of analog-year precipitation prediction methods have been explored (e.g., Saha et al., 2014; Zhang et al., 2007). Although such models display some prediction skills, their predictability is limited due to the complex relationship between

precipitation and the known teleconnections (e.g., Folland et al., 1991; Gershunov, 1998; Obled et al., 2002; Rajeevan et al., 2007).

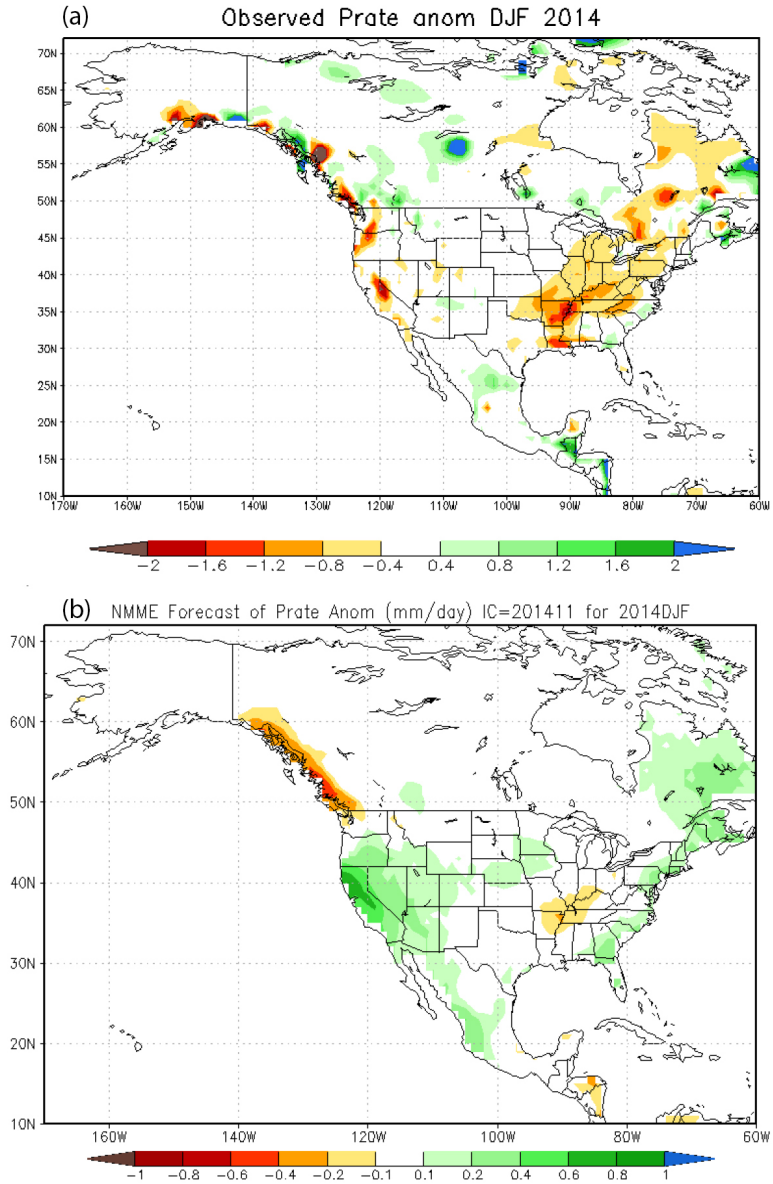

Fig. 3: Comparison between a) the observed precipitation and b) the NMME simulation for the anomalies of the precipitation rate from Dec, 2014 to Feb, 2015. The forecast initial condition is set to Oct, 2014. Note that the color bars in the maps are not in the same scale.

Physically based dynamical models have also been explored for seasonal precipitation prediction. Unlike statistical techniques, these models rely on the dynamical interactions among the land, ocean, and atmosphere, which are resolved using model parameterization and numerical simulations (e.g., Zhang et al., 2007; Merryfield et al., 2013; Saha et al., 2014). Progress in dynamical model simulations over the past three decades has led to better and more reliable predictions. However, the predictability of dynamical model simulations is still rather limited

and is highly variable in space and time (Yang et al., 2009; Wang et al., 2009; Kim et al., 2012; Infanti and Kirtman, 2015; Jia et al., 2015). Previous studies have shown that the forecasting skill of dynamical models is mainly explained by the El Nino-Southern Oscillation (ENSO) variability (Kumar et al., 2007; Wang et al., 2009; Cohen and Jones, 2011), which itself does not fully account for the total variability in precipitation (Gao et al., 2006). To overcome the limitations of individual dynamical models and benefit from the strength of a diverse set of models, there has been a growing tendency to use multiple models and combine their forecasts (Hewitt 2004; Palmer et al, 2004; Bougeault, 2010). Recently, a multi-agency effort led to the development of the North American Multi-Model Ensemble (NMME; Kirtman et al., 2014), which has provided climate forecasts ranging from intra-seasonal to inter-seasonal scales. The NMME ensemble average generally offers better predictions than individual contributing models do for different regions (Becker et al., 2014; Kirtman et al., 2014; Ma et al., 2015); however, the reliability of the precipitation forecasts in general is still rather low (Becker et al., 2014; Kirtman et al., 2014). As an example, Figure 3 shows the observed and NMME-predicted anomalies for Dec. 2014-Feb. 2015 precipitation (DJF 2014), from a forecast initial condition in October 2014. As shown, the NMME's precipitation prediction for DJF 2014 was not consistent with the observations in the western US (i.e., the NMME indicated a positive precipitation anomaly, but the region experienced one of its most extreme droughts). Similar maps based on different initialization dates can be found through Climate Prediction Center (http://www.cpc.ncep.noaa.gov/products/NMME/http://www.cpc.ncep.noaa.gov/products/NMME/).

Previous studies have argued that combining statistical and dynamical models can improve seasonal precipitation prediction (Coelho et al., 2004; Schepen et al., 2012). This study outlines a hybrid framework for combining dynamical and statistical seasonal precipitation forecasts to improve their skill, with consequent benefits for improved drought prediction in the southwest US and other regions. The proposed hybrid framework is fundamentally different from the statistical post-processing approaches in which a statistical model is used to combine multiple dynamical models, e.g., by weighing the ensemble members (Raftery et al., 2005; Luo et al., 2007; Schepen and Wang, 2013). It follows instead a hierarchical approach also taken by Schepen et al. (2014), where dynamical and statistical models work in parallel and offer their own predictions, and are subsequently merged into a single prediction. Here, the dynamical component is based on the available NMME simulations. The statistical forecasts employ a Bayesian analog-year approach that simulates precipitation based on a number of conditioning factors, such as the Pacific Decadal Oscillation (PDO), Multivariate ENSO Index (MEI), and Atlantic Multidecadal Oscillation (AMO). The statistical analog-year forecasts and the NMME dynamical model simulations are then combined via a multi-model averaging framework. In contrast to the conventional ensemble mean, the weighted averaging techniques such as Bayesian-based techniques (Raftery et al., 2005; Buser et al., 2010; Najafi and Moradkhani, 2015) and expert-based algorithms (Cheng and AghaKouchak, 2015) distribute the weights based on the performance of each model during a training period. The final ensemble response

from weighted averaging techniques generally outperforms the single best model (Weigel et al., 2008) and the simple ensemble mean, except under particular circumstances such as extremely large variability in models (Weigel et al., 2010). This study uses the so-called Expert Advice (hereafter, EA) algorithm described in Cheng and AghaKouchak (2015), which returns the weighted average of the ensemble that is supposedly the best response from the ensemble of statistical and dynamical simulations.

Study Area and Data Resources

This study focuses on seasonal precipitation forecasting in California and Nevada. This region has recently suffered from severe droughts, and reliable forecasts have become crucial for improving water management. In California, 75% of the annual precipitation occurs between November and March (i.e., rainy season), with the half occurring between December and February (Shukla et al., 2015). Given the strong seasonality of precipitation in the region, water management primarily relies on rainy season precipitation. Thus, this study focuses on precipitation forecasting during the rainy season with different lead times. The forecast periods begin from November, December, and January of each year and continues to March; that is, 3- to 5-month lead times (i.e., NDJ, NDJF, NDJFM, DJF, DJFM, and JFM). All forecasts are initiated on October.

This study proposes a hybrid method to improve precipitation forecasts by combining predictions based on the dynamical model simulations with statistical predictions that leverage atmosphere-ocean teleconnections with the seasonal precipitation. The dynamical model simulations with different lead times are obtained from the North American Multi Model Ensemble (NMME; Kirtman et al, 2014). Retrospective NMME simulations for Jan. 1982 – Dec. 2010 are available at the International Research Institute for Climate and Society (IRI)'s climate data library. Real-time forecasts of NMME are also available since Aug. 2011 except a few models (CMC1-CanCM3 and CMC2-CanCM4), which are available since December 2011. To avoid discrepancies in the number of models form one year to another, we excluded 2011 simulations from our analysis and used the rest of data during 1982-2014 for which all model simulations were available. The observed reference precipitation is based on a gridded station-based data record developed for western US forecasting and verification purposes (Wood 2008; Tang et al., 2009).

Hybrid Forecast Model

This study proposes a hybrid precipitation prediction framework that combines the dynamical NMME forecasts with statistical simulations in each 1x1 degree grid cell across the study area. The purpose of combining these two types of models is to select the best forecasts from the ensemble of dynamical and statistical predictions. Figure 4 shows an overview of the proposed hybrid precipitation prediction model. The dynamical (panel (a) in Fig. 4) and statistical (panels (b) in Fig. 4) simulations run in parallel; each leads to an ensemble of predictions. Then, the forecast ensembles produced from the dynamical and statistical model

simulations are overlaid to form the final ensemble (panel (c) in Fig. 4). Lastly, the EA algorithm, trained with model performance in the past, finds the best ensemble response from the statistical and dynamical predictions (panel (d) in Fig. 4).

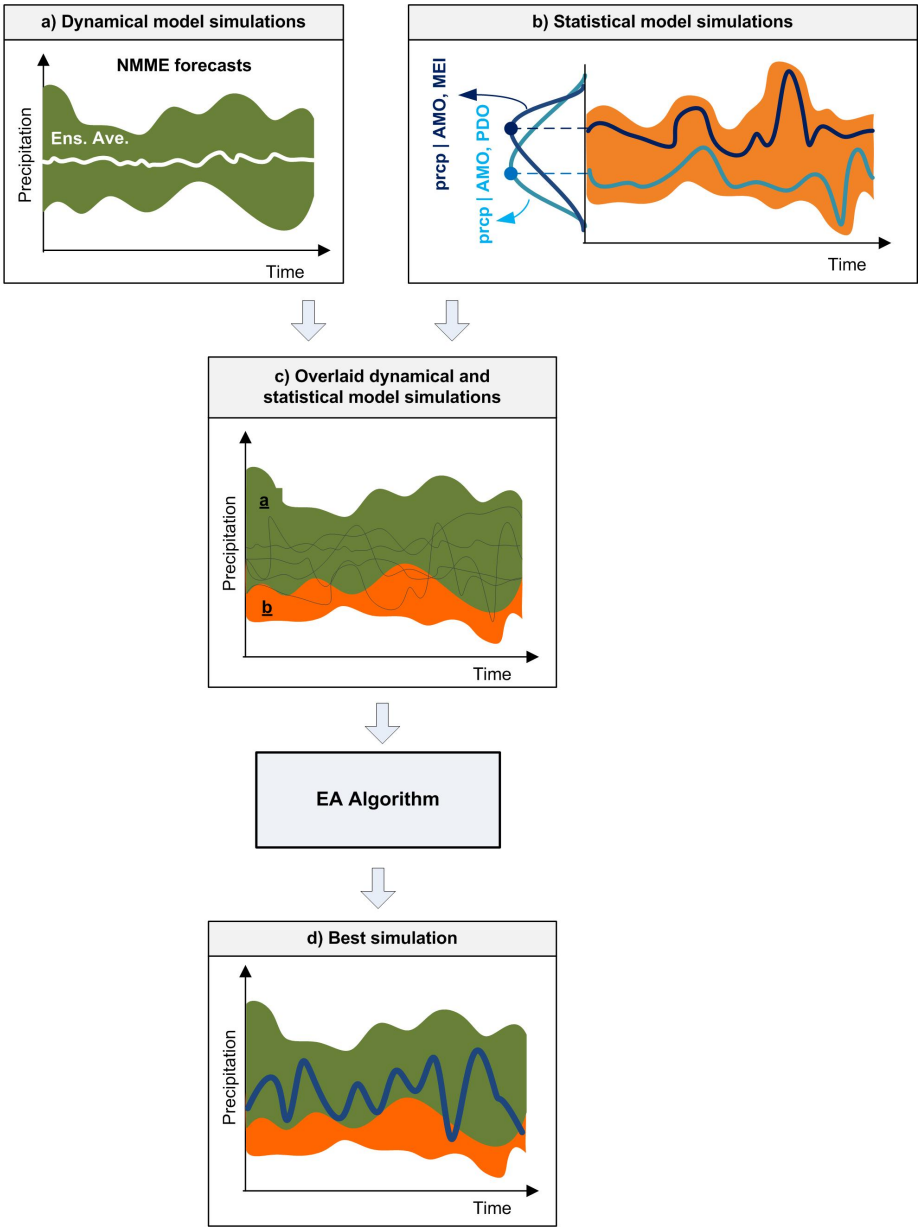

Fig. 4: Flowchart of the proposed hybrid statistical-dynamical precipitation forecasting algorithm. See the text for details.

a) Dynamical Model Simulations

The North America Multi-Model Ensemble (NMME; Kirtman et al., 2014) is an ensemble of simulations from multiple dynamical models and provides probabilistic forecasts with some information regarding forecast uncertainty. Each dynamical model contributes a certain number of ensemble members. In this study, we picked an ensemble of 99 members from eight models which are used by the Climate Prediction Center (CPC) for the operational forecasts (i.e.,

CMC1-CanCM3 [10], CMC2-CanCM4 [10], COLA-RSMAS-CCSM4 [10], GFDL-CM2p1-aer04 [10], GFDL-CM2p5-FLOR-A06 [12], GFDL-CM2p5-FLOR-B01 [12], NASA-GMAO-062012 [11], NCEP-CFSv2 [24]) and used the ensemble mean of each model in the hybrid forecast model that is discussed in following sections. We studied the NMME precipitation forecasts beginning from November (initialized in October) with up to a 5-month lead time (i.e., November – March, NDJFM) during 1982-2014, except the year 2011 since some NMME models' data are not available for 2011. This is the rainy season for the study area.

b) Statistical Analog-Year Simulations

Several studies have discussed the impacts of atmosphere-ocean teleconnections on seasonal precipitation patterns (Rasmusson and Wallace, 1983; Ropelewski and Halpert, 1986; Bradley et al., 1987; McCabe and Dettinger, 1999; Kurtzman and Scanlon, 2007; DeFlorio, 2013). The ENSO, which represents the fluctuation of sea surface temperature (SST) and air pressure in the tropical eastern Pacific Ocean, affects regional precipitation levels, across several regions of the globe including North America (Bradley et al., 1987; Redmond and Koch, 1991; Diaz and Kiladis, 1992). The above-normal SST (warm phase or El Nino) and below-normal SST (cold phase or La Nina) in the tropical Pacific Ocean have different climatic impacts (Bradley et al., 1987; Hoerling et al., 1997; Trenberth, 1984, 1997) with variable significance, depending on the signal's strength (Kiladis and Diaz, 1989; Redmond and Koch, 1991). For instance, the above-normal precipitation in southern California is usually associated with El Nino episodes (Redmond and Koch, 1991), whereas precipitation over northern California does not show a strong association with either El Nino or La Nina episodes (McCabe and Dettinger, 1999). However, the collective information from ENSO signals and the long-term fluctuations in the North Pacific Ocean-indicated as the Pacific Decadal Oscillation (PDO) can improve the precipitation prediction skill in the western US (McCabe and Dettinger, 1999). In addition, the Atlantic Multidecadal Oscillation (AMO), which reflects the long-term changes in the sea surface temperature of the North Atlantic Ocean, affects precipitation and drought frequency over North America (McCabe et al., 2004). The two major droughts in the 20th century (1930s and 1950s) occurred during the positive phase of AMO and negative phase of PDO between 1925 and 1965 (McCabe et al., 2004). Given the demonstrated capability of PDO, MEI, and AMO in the prediction of precipitation over North America, this study assesses the potential for these three indices to improve seasonal precipitation forecasts over Southwest US. The monthly records of teleconnection indices are obtained from the Earth System Research Laboratory at the National Oceanic and Atmospheric Administration (NOAA). More information on PDO, MEI, and AMO and their impacts on the southwestern US is provided in Appendix A.

The proposed hybrid approach benefits from the predictability of an analog-year model based on teleconnection indices (Hidalgo and Dracup, 2003; Kurtzman and Scanlon, 2007). We propose a Bayesian model based on copula functions (Joe, 1997; Nelsen, 1999) to represent the joint distribution of teleconnection indices and seasonal precipitation. Unlike multivariate distribution functions, such as the bivariate Gaussian or Gamma distributions (Kelly and

Krzysztofowicz, 1997; Sharma, 2000; Yue et al., 2001), copulas do not require all of the marginal distributions to come from the same distribution.

Copula functions are defined as multivariate distribution functions, $\mathrm{P}(\mathrm{x}_1, \ldots, \mathrm{x}_\mathrm{n})$, with uniformly distributed variables on the interval $[0, 1]$:

$$P(x_1, \ldots, x_i, \ldots, x_n) = C[P(x_1), \ldots, P(x_i), \ldots, P(x_n)] = C(u_1, \ldots, u_i, \ldots, u_n) \quad (1)$$

where, C is the Cumulative Distribution Function (CDF) of the copula, and $P(x_i)$ is the marginal distribution of x_i being uniform on the interval $[0, 1]$, which is also denoted by u_i. Note that C connects the CDFs of the random variables (i.e., u_i), whereas $P(\ldots)$ in the left-hand side represents the joint probabilities of the original random variables (i.e., x_i).

The Elliptical and Archimedean copulas (Embrechts et al., 2003; Nelsen, 1999) are the two families that are most frequently used in hydrologic applications (e.g., Favre et al., 2004; Dupuis, 2007; Hao and AghaKouchak, 2013; Madadgar and Moradkhani, 2015). Archimedean copulas have limitations in preserving high dimensional pair-wise dependence (Joe 1997). Elliptical copulas, on the other hand, are more flexible for describing associations among more than two variables. For this reason, we use Gaussian copula from the elliptical family for the analog-year model as explained below.

We use the conditional probability distribution function based on copulas (Madadgar and Moradkhani, 2013) to estimate the predictive distribution of precipitation given the joint status of the teleconnection indices:

$$p(x_1 | \, x_2 \; \ldots, x_n) = \frac{c(u_1, \ldots, u_n) \prod_{i=1}^{n} p(x_i)}{c(u_2, \ldots, u_n) \prod_{i=2}^{n} p(x_i)} \quad (2)$$

where, $p(x_1 | \, x_2 \; \ldots, x_n)$ is the conditional distribution of the random variable x_1 given the set $(x_2 \; \ldots, x_n)$ of random variables; $c(u_1, \ldots, u_n)$ is the Probability Density Function (PDF) of the continuous copula function; and $p(x_i)$ is the PDF of ith random variable. The conditional probability of x_1 given x_2 (i.e., bivariate case) is expressed as follows:

$$p(x_1 | x_2) = c(u_1, u_2).p(x_1) \quad (3)$$

In a trivariate case, the conditional probability of x_1 given $\mathrm{x}_2, \mathrm{x}_3$ is defined as

$$p(x_1 | x_2, x_3) = \frac{c(u_1, u_2, u_3).p(x_1)}{c(u_2, u_3)} \quad (4)$$

We used Eq. 4 to estimate the conditional probability of precipitation at each grid cell in the study area (denoted by x_1) given multiple teleconnection indices (denoted by x_2 and x_3) that have been observed in the preceding months/seasons. We have used multiple variables, including PDO, MEI, and AMO, and linked them to precipitation using Gaussian copula as mentioned above. The copula parameters have been estimated using the method of Inference Function for Margins (IFM; Joe, 1997). The predictive distribution of Eq. 4 is then obtained once using AMO

(i.e. x_2) and MEI (i.e. x_3) and once using AMO (i.e. x_2) and PDO (i.e. x_3). Then, the 50th percentiles (median) of the resulting probability distributions are used as the final forecasts; that is, two forecasts each obtained from a separate probability distribution.

c) Expert Advice (EA) Algorithm

In the hybrid model, the Expert Advice (EA) algorithm (Cheng and AghaKouchak, 2015) is used to combine the dynamical and analog-year statistical components (Fig. 4). In this application, the final ensemble in the hybrid model consists of the two statistical analog-year model predictions, the grand ensemble mean of the NMME forecasts, and the ensemble mean of each participating model in the NMME- that is, eight ensemble members from eight models – making a total of eleven inputs to the EA algorithm. The EA algorithm assigns different weights to the ensemble members based on their performance during a training period, and returns their weighted average as the best ensemble response.

Previous studies show that averaging the ensemble of multi-model predictions with equal weights does not necessarily lead to the most skillful outcome (Masson and Knutti, 2011; Knutti et al., 2010). In fact, the ensemble mean may be biased by poorly performing models (Krishnamurti et al., 2000) and smooth out the extreme events predictions (panel (a) in Fig. 4). The EA algorithm argues that instead of the ensemble mean, an ensemble response should be selected that is better than each individual ensemble member, plus an error term. The EA algorithm starts with equal weights ($w_0^1, w_0^2, \ldots, w_0^N = \frac{1}{N}$) for all the N ensemble members (including both statistical and dynamical simulations) at the first time step ($t = 1$) of the training period (see Figure 5). In this particular application of the method, there are 11 weights (i.e. $N = 11$) for 11 forecast components at each time step ($\gamma^{n,t}$) (i.e. the 8 dynamical model ensemble means, the NMME grand ensemble mean, and the two statistical predictions). The weight of each member is then updated at each time step based on its relative performance to the others during the past time steps. A loss (error) function, $\lambda(\omega, \gamma)$, is used to adjust the weights of ensemble members based on the observed variable (i.e. ω) and the simulated variable (i.e. γ). The loss function is obtained by optimizing the weight function $\phi_t(\omega)$ as explained in Vovk (2001).. Ultimately, the goal of the algorithm is to find the best ensemble response (Fig. 5-b) with the smallest cumulative error over the training period. More details on EA algorithm is found in Cheng and AghaKouchak (2015). Given the relatively short length of record (1982-2014), we use hindcasts from 1982 up to the last year before the target year (after 2005) for estimating the weights (i.e. training purposes). The model is then validated for the target year based on ground-based observations.

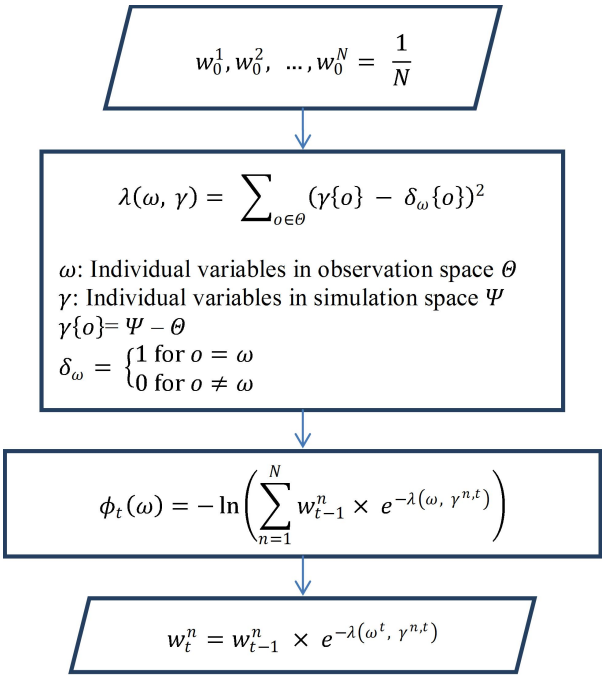

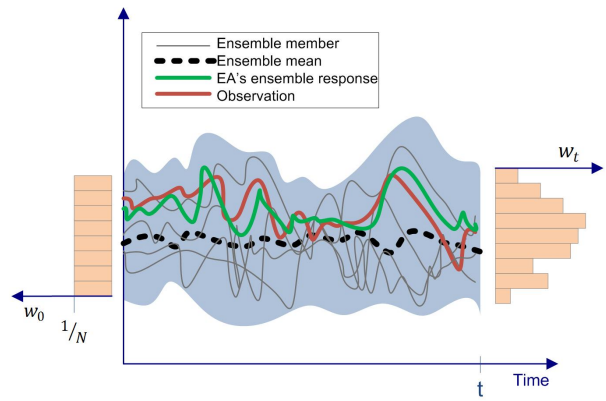

Fig. 5: The flowchart (a) and schematic view (b) of the Expert Advice (EA) algorithm.

Results and Discussion

In this section, we show the results of the proposed hybrid precipitation prediction approach at the spatial resolution of 1 x 1 degree over the southwest US. Precipitation forecasts are presented for different periods during the rainy season of the region; i.e. NDJ, NDJF, NDJFM, DJF, DJFM, and JFM. The results of the statistical precipitation model are also generated for the same forecast periods. This step involves the conditional forecast of precipitation anomaly given the global teleconnection indices, including PDO, MEI, and AMO. The statistical model describes the joint relationship between AMO-MEI (and AMO-PDO) and winter precipitation using copulas (see also Eq. 4). These climate indices are averaged over Jun-Oct where they show relatively high correlation with the following rainy season precipitation in several regions of the world (Schepen et al., 2012; Khedun et., 2014; Kurtzman and Scanlon, 2007) including the western US (Redmond and Koch, 1991). It should be noted that there are some sources of uncertainty in reported climate indices such as PDO (Wen et al., 2014) which can influence the relationships between the predictors and precipitation to some extend and consequently affect the statistical model simulations. As explained earlier, the conditional PDF of precipitation was separately estimated for each pair of teleconnection indices (see Eq. 4), and the 50th percentile (median) is used as the final prediction of associated PDF. The choice of 50th percentile from the predictive distribution is another source of uncertainty in statistical model simulations which needs to be studied in future efforts.

The EA algorithm is applied to both statistical model simulations and dynamical model simulations. To evaluate the proposed hybrid framework, we assessed the predictability of the hybrid model and the dynamical model in capturing the negative precipitation anomalies (below-

average precipitation) during two major droughts in the past decade; 2006-2008 and 2012-2014. Note that precipitation anomalies for each forecast period at each grid cell are calculated based on the average precipitation over 1982-2014 in that particular grid cell.

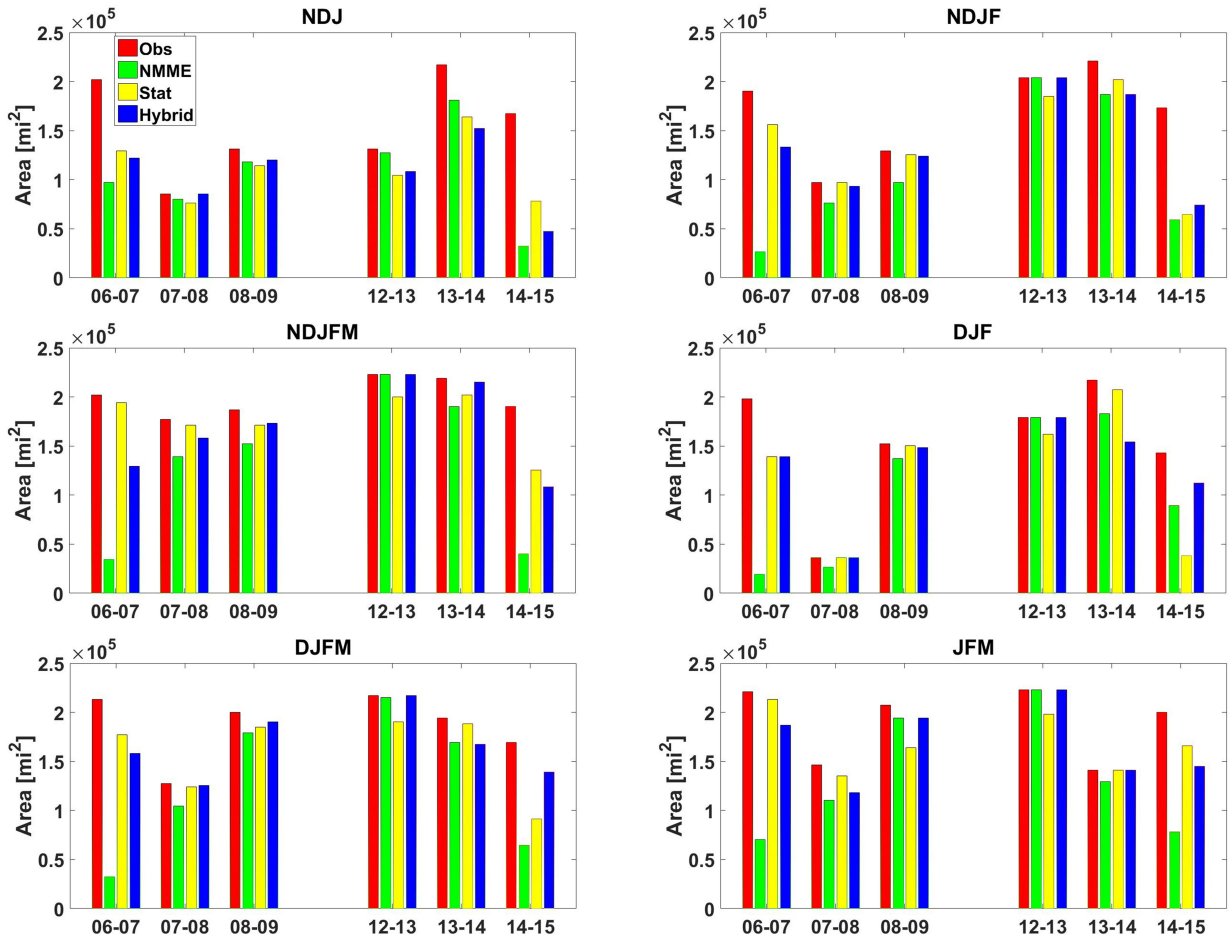

Fig. 6: The area [mi^2] with the observed negative precipitation anomaly (red bars) correctly captured by the NMME (green bars), statistical model (yellow bars), and hybrid model (blue bars) predictions during 2006-2008 and 2012-2014 droughts. Forecasts are initiated from October of each year, i.e. IC = Oct and the target forecast periods start at Nov, Dec, or Jan and continues up to the following March.

Figure 6 shows the size of observed area under drought conditions (i.e. negative precipitation anomaly) (light gray bars) and the size of area correctly captured as dry region using the grand ensemble mean of the NMME (dark gray bars), the statistical simulations' mean (yellow bars), and the hybrid framework (blue bars). Note that the size of area is calculated based on the total number of grid cells with observed/simulated negative precipitation anomaly multiplied by the size of each grid cell. As shown, the hybrid model and the statistical model could capture these two drought events better than NMME, especially for the rainy season of 2006-7 and 2014-15. The drought predictability for 2014-15 varies from 28% (NDJ) to 82% (DJFM) for the hybrid

model, and 19% (NDJ) to 62% (DJF) for the NMME model. Overall, for the extreme drought of 2014-15, the predictability of hybrid model was 10% (NDJ, NDJF) to 50% (DJFM) greater than that of NMME. Similarly, for 2006-7 drought, the predictability increases by 10% (NDJ) to 60% (NDJF, DJF, DJFM) after the hybrid-model application. Note that in some other years all the three models could successfully capture drought conditions across the region and their drought predictabilities were rather similar (Figure 6).

Figures 7a and 7b display the spatial distribution of the observed precipitation anomaly (1st column), ensemble mean of NMME forecasts (2nd column), the statistical simulations' mean (3rd column), and the hybrid simulation (4th column) during the rainy season of 2006-7 (Figure 7a) and 2014-15 (Figure 7b). The pixels with a positive precipitation anomaly are shown in blue, and those with a negative anomaly are shown in brown. For each target year (e.g., 2006-7 and 2014-15), we used the data from 1982 up to the last year before target year to calibrate the hybrid-model parameters, including the weights of the EA algorithm and the copula parameters. This procedure was repeated for each target year at each grid cell (1 x 1 degree).

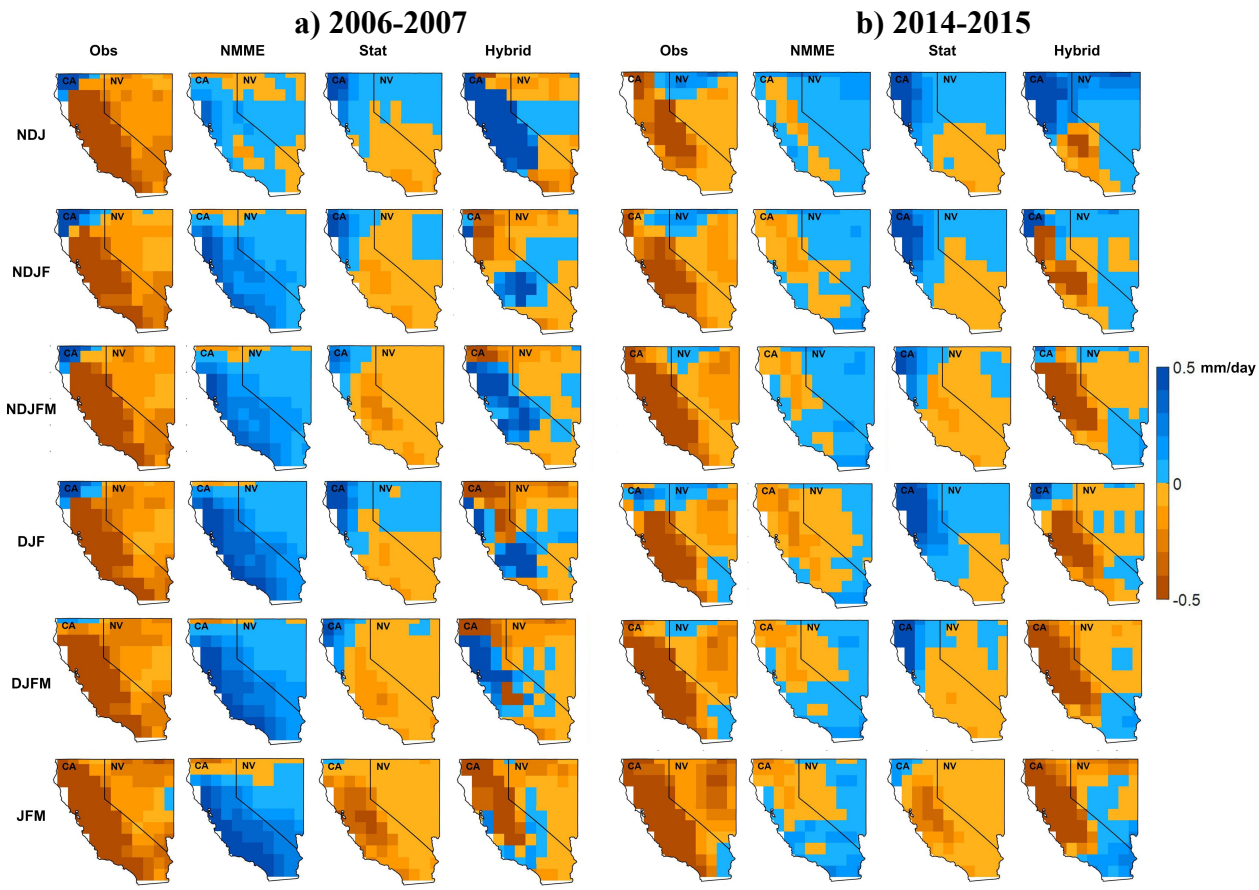

Fig. 7: Precipitation anomaly (mm/day) during the rainy season of a) 2006-2007 and b) 2014-2015 (right) with different lead times (NDJ, NDJF, NDJFM, DJF, DJFM, and JFM). Forecasts are initiated from October of each year, i.e. IC = Oct. The observations (1st col. from left), NMME forecasts (2nd col.), statistical model predictions (3rd col.), and hybrid model predictions (4th col.) are shown for the target periods of each year.

As shown in the observations, the southwestern US has experienced extreme droughts in 2006-2008 and 2012-2014 periods, specifically in the latter. As shown for 2006-7 period, the NMME signal was opposite of that of the observations in all the lead times (i.e., NMME indicated wet conditions, but the region experienced a major drought). However, both the statistical model and the hybrid model could capture the 2006-7 drought much better than NMME. Despite the performance of statistical model, its contribution in the final hybrid model depends on its performance during the entire training period. Likewise, the contribution of the hybrid model depends on its performance during the training period. According to the final weights of statistical and dynamical models, both statistical and dynamical models contribute in the final result of the hybrid model. Although some discrepancies between the hybrid model and the observations are apparent in central California, the overall performance of the hybrid model is better than using solely dynamical or statistical model simulations in capturing the drought of 2006-7 across the region. In 2014-15, the NMME could capture the negative anomalies in most parts of California (especially in NDJF and DJF); however, it gives opposite signal for almost entire Nevada. The statistical model, on the other hand, could predict the negative anomalies of the southern part of the region and fails to capture the drought conditions in the northern part. The combination of the two models (i.e. the hybrid model), however, could improve the predictions of the NMME and statistical model for most parts of the region.

This study also analyzes the performance of the three models for the wet winter of 2010-2011 (i.e. 2010-11). Figure 8 compares the predictions of the NMME, statistical model, and the proposed hybrid statistical-dynamical model for the rainy season of 2010-11. Similar to the previous results, the forecast lead time increases from 3 months to 5 months. As shown, the statistical model could not predict the positive anomalies in the region. The grand ensemble mean of NMME forecasts also failed to represent the positive precipitation anomalies (i.e. wet conditions) especially in central and south California. However, the hybrid model slightly improved the predictions for central California and Nevada (Fig. 8-a). The predictability of wet conditions in 2010-11 varies from 45% (NDJFM) to 85% (JFM) for the hybrid model and from 35% (NDJ) to 60% (JFM) for the NMME. Overall, the hybrid model improves the predictability (Fig. 8-b) by 5% (DJFM) to 25% (JFM) relative to the NMME. Comparing the results in Fig. 6-8 indicates that all the three models have higher predictability in the selected dry years than in the selected wet year. It should be noted that the wet conditions in 2010-11 was significantly attributed to a sequence of Atmospheric River (AR) storms (Zhu and Newell, 1998). AR storms are generated by water-vapor streams in the atmosphere and usually supply approximately 20-50% of the annual precipitation and streamflow in California (Dettinger, 2013). In December 2010, ARs occurred within a week's time and provided half of the average annual precipitation for central and southern California. Although some connections are found between ARs and atmosphere-ocean dynamics such as Madden-Julian Oscillation (MJO) (Guan et al., 2012; Ralph et al., 2011), North Atlantic Oscillation (NAO) (Lavers and Villarini, 2013), Arctic Oscillation (AO) and Pacific North American Index (PNA) (Guan et al., 2013), these associations are not yet

clearly understood (Gimeno et al., 2014), and operate at sub-seasonal rather than seasonal time scales. Predicting ARs is very challenging, and both dynamical and statistical models have limitations in representing them. This is one of the limitations of the proposed hybrid statistical-dynamical framework and can be improved if the dynamical and statistical models provide more accurate simulations of the ARs, or if other teleconnection indices are discovered that more strongly reflect a tendency for ARs within a given season.

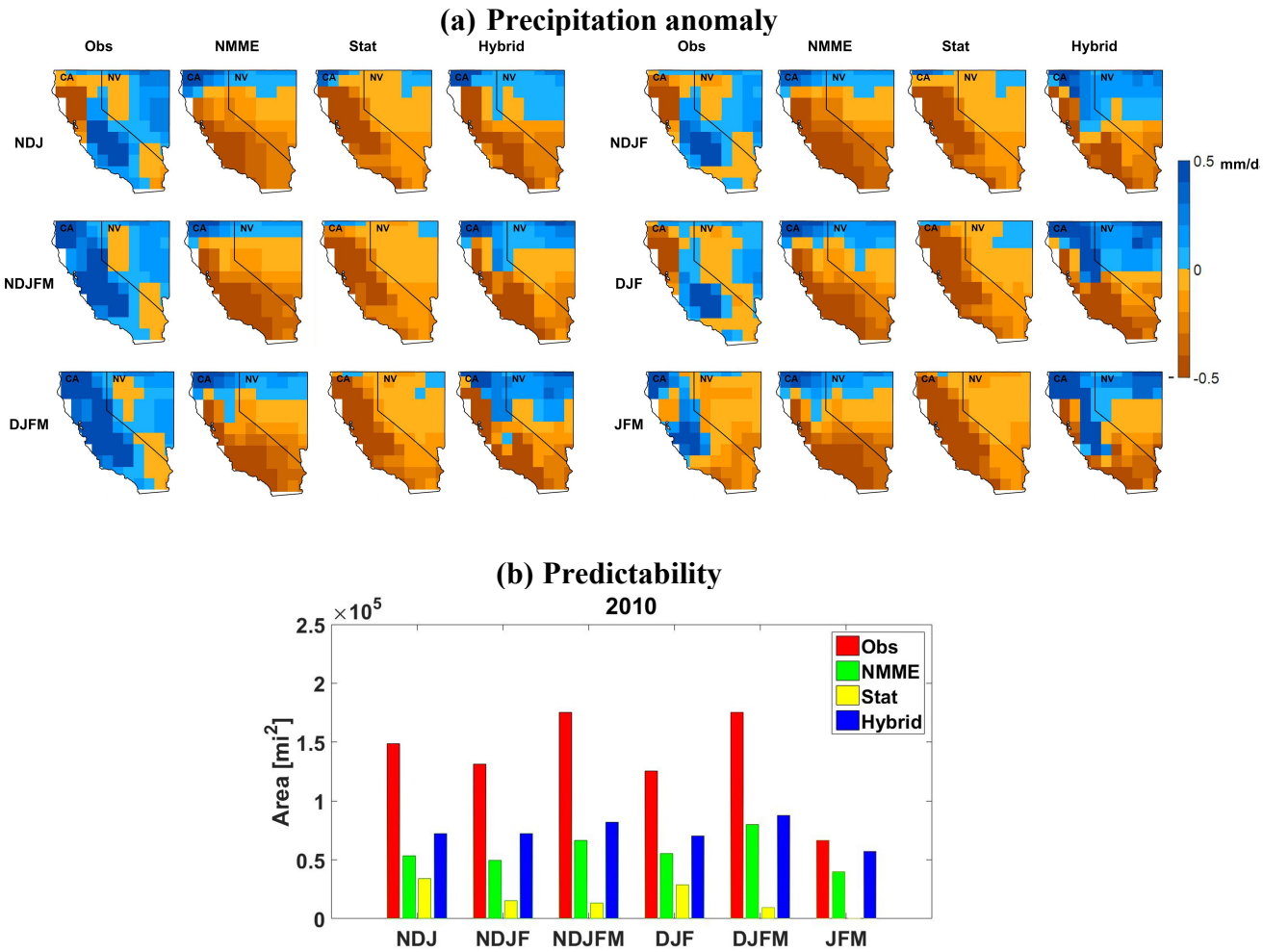

Fig. 8: Comparing the performance of hybrid model and the dynamical and statistical models in a) capturing the positive precipitation anomalies (i.e. wet conditions) and b) predictability of positive anomalies during the rainy season of 2010-2011.

Insight into the contributions of the different components of the hybrid framework can be gained from assessing the weights obtained for the statistical and dynamical forecasts, for different seasonal predictands. Figure 9 displays the spatial distribution of weights obtained from the EA algorithm for the grand ensemble mean of the NMME and the statistical model simulations. As seen, the ensemble mean of the NMME attained generally larger weights in northern California relative to the statistical model simulations. In contrast, the statistical model simulations obtained larger weights in southern California and central to southern Nevada.

Neither model, however, receives large weights in central California and northern Nevada, which means that the rest of ensemble members (corresponding to the ensemble mean of each of the eight NMME models) in the hybrid model ensemble are given large weights for those regions.

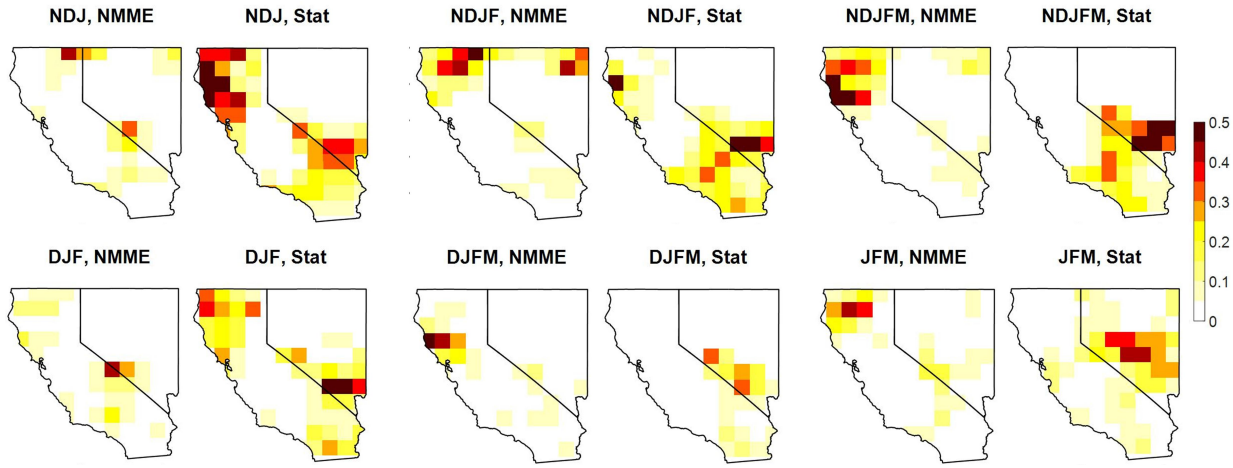

Fig. 9: Weight distribution obtained from the EA algorithm for the NMME ensemble mean forecasts (left) and the statistical model forecasts (right) for different prediction periods (i.e. NDJ, NDJF, NDJFM, DJF, DJFM, JFM).

Concluding remarks

In recent decades, drought monitoring has improved significantly due to a range of satellite observations and hydroclimate reanalysis datasets (Xia et al., 2012). However, drought prediction at seasonal to inter-annual scales remains a grand challenge at a regional scale, as evidenced by forecasts during the recent drought in the western US (Seager et al., 2014). A breakthrough in predicting precipitation can lead to major improvements in water management and risk reduction. This study presents a hybrid seasonal climate forecasting approach that combines physically based dynamical models and statistical models, and investigates its potential for improving drought prediction in the southwestern US. The proposed hybrid model combines dynamical model forecasts from the NMME with Bayesian statistical forecasts using teleconnections indices (PDO, MEI, and AMO). The hybrid model utilizes the EA algorithm to merge the dynamical model forecasts and statistical model predictions. The hybrid method aims to improve drought prediction by combining these two fundamentally different seasonal precipitation prediction methods.

The results indicate that although the dynamical model simulations capture some of the recent droughts, they do not offer high predictability, corroborating prior assessments of dynamical model precipitation prediction skill. The integration of the statistical and dynamical methods, however, appears to improve the prediction of seasonal precipitation in this case study. The predictability of seasonal precipitation increases by 5-60% after the application of hybrid model. Overall, the hybrid framework performs better in predicting below-normal precipitation than above-normal precipitation. While there are still major challenges for reliable seasonal drought predictions, the results of this study encourage further exploration of hybrid dynamical-statistical methods in different regions with different climate regimes. We acknowledge that several issues

such as the relatively short record, uncertainty in the observed dependencies, and model parameterization may have affected predictions of wet and drought anomalies. More efforts and evaluations of the proposed model are required before this model can be used in water resources management.

Drought prediction studies often focus on national or continental-scale predictions with less attention to their adequacy for regional conditions and impacts. The manifestation of drought impacts at very local to regional scales, however, motivates interest in evaluating drought-related prediction approaches at local to regional scales. At regional scales, different sources of predictability may be harnessed through different forecasting methods. For instance, the strength of climate indices (e.g., ENSO) influence on local climate varies in different regions and seasons, and dynamical climate forecasting model performance varies similarly. Here, the hybrid model is applied for the southwestern US by including climatic indicators that have been shown to affect precipitation in this region. This modeling framework can potentially be applied to other regions by integrating the relevant region-specific climatic indicators, as well as the NMME predictions that have a global extent.

(IV) Amplified warming of droughts in the historical record and climate model projections

During droughts, low surface moisture may translate surface heating into warming, since excess energy will be converted into sensible heat instead of evaporating as latent heat. Recent concurrent occurrences of droughts and heatwaves have caused compounding ecosystem and societal stresses, which prompted our investigation of whether there has been a shift in temperatures under meteorological drought conditions in the United States. Strong feedbacks between drought conditions and surface temperatures prompted our investigation of whether droughts have been warming faster than average climate conditions in the United States. Using historical observations, we detected that droughts have been warming faster than the average climate in southern and northeastern U.S. Climate model projections also showed a pronounced warming shift in southern states between the late 20th and 21st centuries. We report that in the southern states, droughts have warmed more than four times the rate at which the average climate has warmed. We argue that the amplified warming is influenced by concurrent changes in vapor pressure deficit and relative humidity, modifying interactions between the land surface and the atmosphere. We anticipate that the magnified shift in temperatures will bring more concurrent extremes in the future, exacerbating individual impacts from high temperatures and droughts.

Key Results

Our study examined shifts in temperatures occurring during dry months to further explore the feedbacks between surface moisture and temperature conditions. Drawing from established interactions between drying and warming conditions, we study whether temperatures during droughts have experienced changes in the 20th century and whether shifts in dry temperatures

will occur under projected climate change conditions. Due to projections showing droughts and high temperatures intensifying over the next century, our goal is to understand whether temperatures are projected to experience different rates of intensification when coupled with dry land conditions.

We evaluate whether historical and climate model datasets have shown evidence of these changes in the contiguous United States. We compare temperatures during different drought severities in two historical [1902-1951 and 1965-2014] and two modeled periods [1951-2000 and 2050-2099]. Since many studies have documented dry regions getting drier and wet regions getting wetter, we explore whether regions with historically dry climate conditions would experience amplified rates of warming in dry conditions.

For our observations, we used monthly temperature and precipitation data available from the Climatic Research Unit, CRU TS3.23, which is a gridded time-series climate dataset [Harris et al., 2014]. The data coverage included all areas of the contiguous United States at a 0.5 degree resolution. We used the bias-corrected spatially disaggregated (BCSD) downscaled Coupled Model Intercomparison Project Phase 5 (CMIP5) multi-model ensemble at a 0.125 degree resolution available from the U.S. Bureau of Reclamation website [Maurer et al., 2007]. We took an average of the models listed in the appendix to form the model ensemble.

We first calculated the average temperature shift associated with each dryness threshold for each pixel. We used the United States Drought Monitor (USDM) classification scheme (D0, D1, D2, etc.) measured by SPI to delineate the drought severity thresholds. For example, at the D0 threshold, we isolated months that had an SPI value of -0.5 or lower and found the corresponding temperature average. To find the temperature shift between periods, we calculated the difference between temperature average associated with each period.

Figure 10a shows that between the early and late 20th century observations from the Climatic Research Unit (CRU), the southern and northeastern U.S. experience higher temperature shifts under dry conditions than the average climate. Figure 10b shows that the southern states display a similar pattern in the downscaled CMIP5 multi-model ensemble.

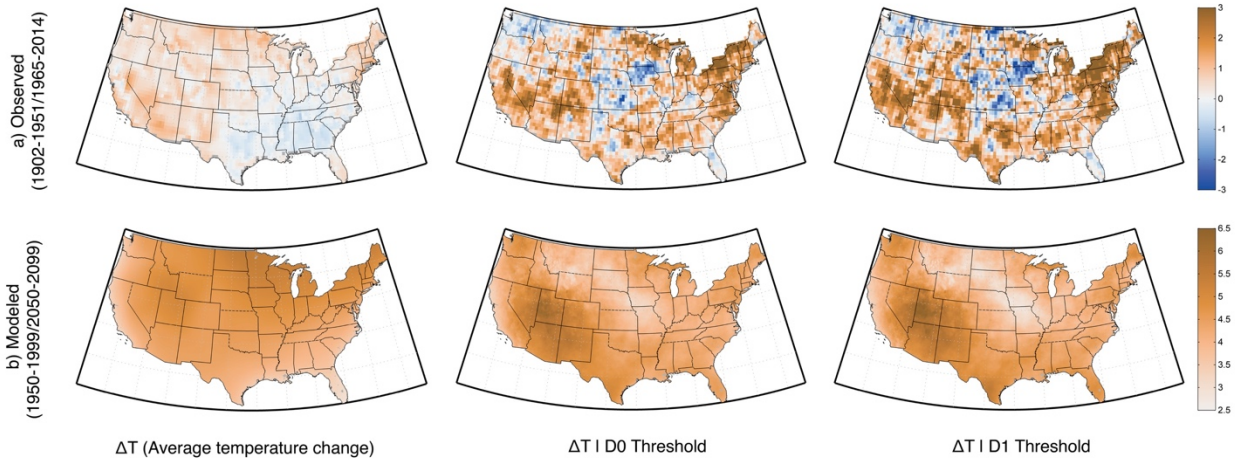

Fig. 10: Temperature shift associated with each dryness condition. Average temperature shift relating to each condition (including all wet and dry conditions, at or under the D0 threshold, at or under the D1 threshold). (A) We compare the period 1965-2014 relative to a baseline period of 1902-1951 with the observed CRU data. (B) We compare the future period 2050-2099 relative to the historical baseline of 1950-1999 with the CMIP5 model average ensemble.

In the observations, the regions associated with amplified temperature change under the D0 and D1 thresholds contrast with the warming regions highlighted in the average temperature change panel, indicating that the pattern is not temperature driven. The accelerated warming seen under dry conditions also does not correspond with regions commonly identified as semi-arid or arid. For example, the southern United States experiences a dry climate in the west and a humid climate in the east; however, all southern states experience similar accelerations in warming under dry conditions. This observation shows that the intensification of dry and wet spatial patterns does not hold true for this concurrent analysis. In the downscaled CMIP5 ensemble, the spatial patterns also do not coincide with the north to south gradient of latitudinal heating predicted under the RCP 8.5 scenario, as shown in Figure 10b. Instead of the northern regions experiencing greater shifts in comparison to the southern regions, our results display the opposite pattern.

The gridded maps of the observed and modeled conditional temperatures display similar patterns in terms of relative change. However, regional delineations in Figures 11 and 12 highlight the differences between the historical observations and model projections. Historically, the northeastern region of the U.S. shows the amplified drought-associated temperature shift, while CMIP5 models predicts a smaller, more muted shift in temperature with respect to the average climate in the entire upper half of the U.S., including the Northeast. CRU observations show that the median dry temperature shifts 0.81 degrees higher than the average climate when we isolate regions with amplified temperature shifts. In the CMIP5 projections, the median dry temperature shifts 0.30 degrees higher than the average climate in the regions with amplified temperature change. The shifts quantified in the observations and models shows the influence of dry periods on the increasing intensity of climate conditions.

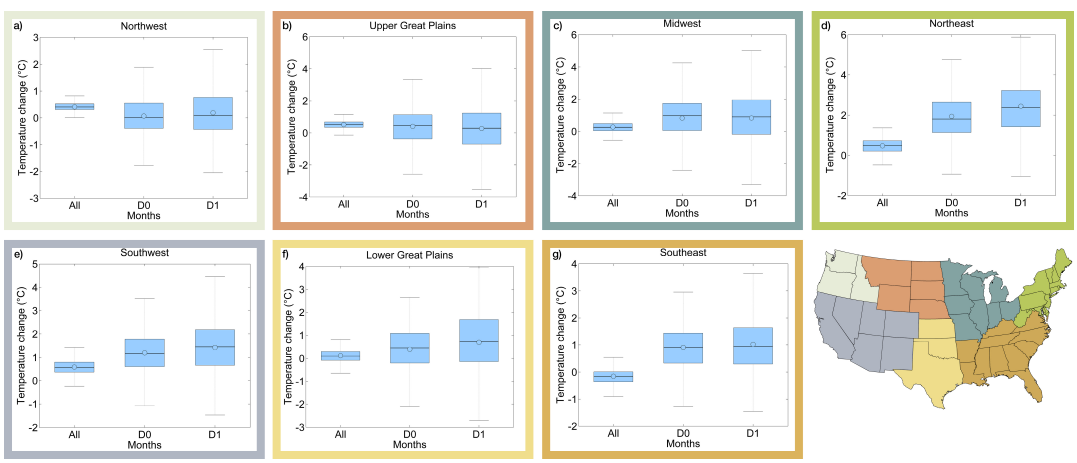

Fig. 11: Regional boxplots for observations. Regional boxplots displaying the temperature shifts corresponding to each dryness condition for the CRU observations [1965-2014 relative to 1902-1951].

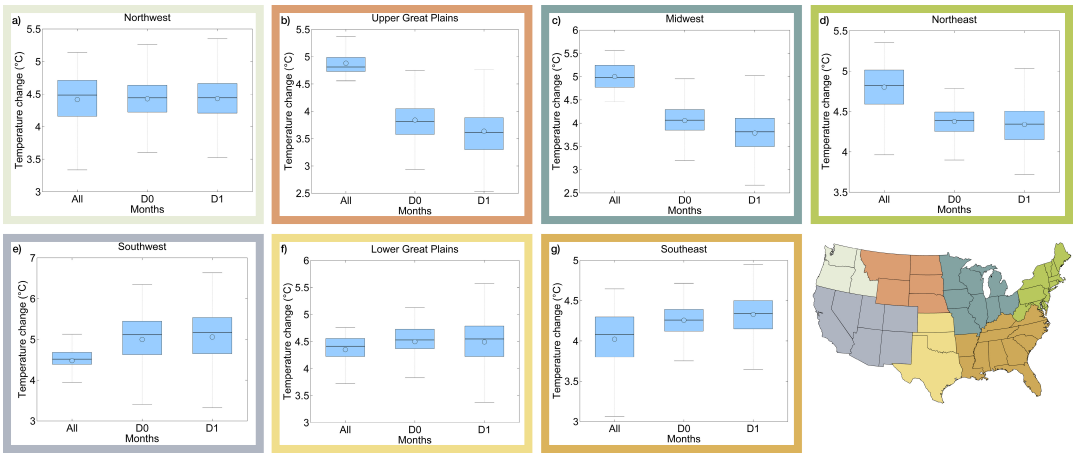

Fig. 12: Regional boxplots for model ensemble. Regional boxplots displaying the temperature shifts corresponding to each dryness condition for the CMIP5 model ensemble [2050-2099 relative to 1950-1999].

Our results show that droughts have been experiencing amplified temperature shifts relative to the average climate in the southern and northeastern regions of the United States. Projections show that droughts will be significantly warmer than average conditions across the southern region of the U.S., associated with modeled shifts in local precipitation and soil moisture. These results help us identify and characterize the increasing intensity of climate conditions under specified dry conditions. The patterns we have associated with waning precipitation and warming temperatures will be important in evaluating and preparing for regional changes in our climate.

(V) Understanding the impacts of future climatic warming on snow water equivalent and water availability in Sierra Nevada.

Summary

Temperature variability impacts the distribution and persistence of the mountain snowpack, which critically provides snowmelt-derived water resources to large populations worldwide. Warmer temperatures decrease the amount of montane snow water equivalent (SWE), forcing its center of mass to higher elevations. We use a unique multivariate probabilistic framework to quantify the response of the 1 April SWE volume and its centroid to a 1.0 to 2.0 °C increase in winter air temperature across the Sierra Nevada (United States). A 1.0 °C increase reduces the probability of exceeding the long-term (1985–2016) average rangewide SWE volume (15.7 km^3) by 20.7%. It correspondingly is 60.6% more likely for the centroid to be higher than its long-term average (2,540 m). We further show that a 1.5 and 2.0 °C increase in the winter temperature reduces the probability of exceeding the long-term average SWE volume by 31.0% and 41.1%, respectively, whereas it becomes 79.3% and 89.8% more likely that the centroid will be higher than 2,540 m for those respective temperature changes. We also characterize regional variability across the Sierra Nevada and show that the northwestern and southeastern regions of the mountain range are 30.3% and 14.0% less likely to have 1 April SWE volumes exceed their long-term average for a 1.0 °C increase about their respective average winter temperatures.

Overall, the SWE in the northern Sierra Nevada exhibits higher hydrologic vulnerability to warming than in the southern region. Given the expected increases in mountain temperatures, the observed rates of change in SWE are expected to intensify in the future.

Evolution of the SWE Volume Centroid

Across the Sierra Nevada, SWE and snowfall have strong regional and elevational signatures. To better understand the spatial variability of the hydrologic risk for various precipitation regimes in the Sierra Nevada [e.g., windward (western) vs. leeward (eastern) sides, higher (southern) vs. lower (northern) elevations, etc.], we divided the 20 basins outlined in Fig. 13A into four study domains: northwest (NW), southwest (SW), northeast (NE), and southeast (SE). Fig. 13B shows the normalized elevational distribution of the drainage area above 1,500 m, which greatly varies by region. Only ~4% and 16% of the area in the NW and NE, respectively, is located above 2,500 m, while 36% and 48% of the area in the SE and SW is located above 2,500 m, respectively. These large areal differences contribute to the regional variability in hydrologic risk associated with the SWE volume and centroid and warming.

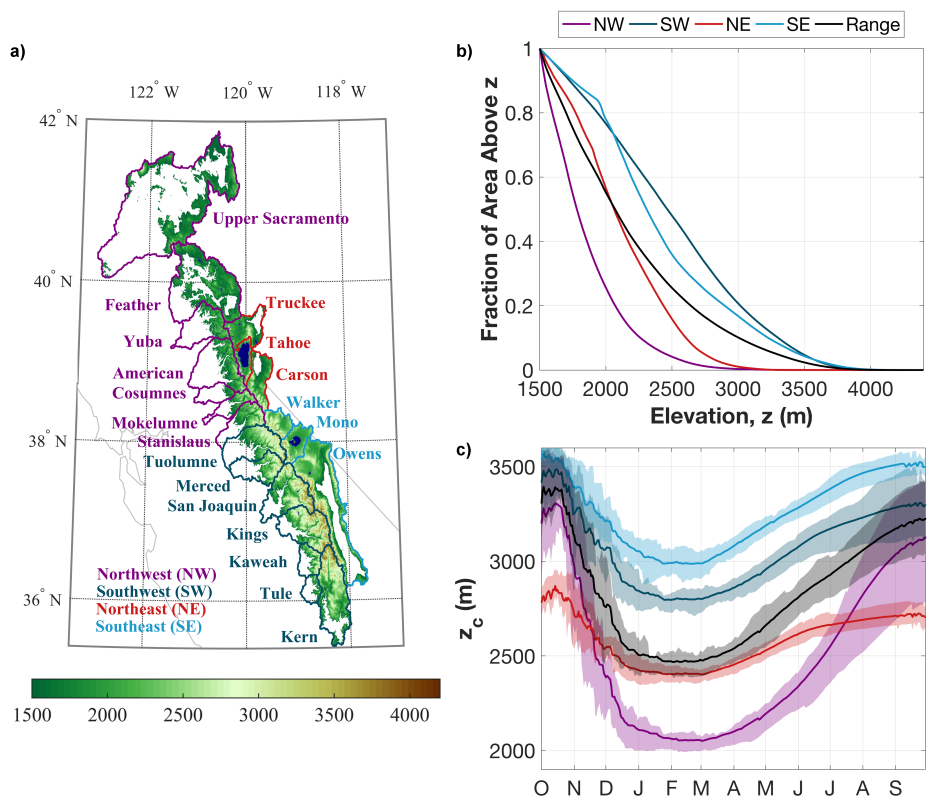

Fig. 13. a) Elevation map showing the Sierra Nevada domain above 1500 m. Color coding denotes regionally grouped basins. This color scheme is used throughout all figures. White pixels are located below 1500 m or outside of the study domain. b) Fraction of area above each elevation (z). c) Temporal movement of the SWE volume centroid (z_c). Long-term average and inter-quartile range of z_c are demarcated by solid lines and shaded areas, respectively. Only pixels above 1500 m were considered in this study.

Although we primarily characterize the 1 April snowpack, Fig. 13C presents the 32-y average time series (solid lines) and interannual variability (shaded areas) of the SWE volume centroid (z_c) from November to August to better understand its location on 1 April relative to other times of the year. Near the start of the accumulation season, the highest elevations receive snowfall causing the SWE volume to be located at these highest elevations. The centroid moves downslope with time as lower elevations receive snowfall and SWE accumulates over a larger area. Minimal variability occurs January–March (Fig. 13C), when temperatures are very cool and storms yield snowfall across nearly all elevations (10). Beginning in the spring (approximately April and May), the interannual variability of z_c begins to increase as low-elevation SWE melts and the centroid recedes toward higher elevations. SWE is again stored at higher elevations in the spring and summer until it melts. Generally, z_c takes on higher elevations in the southern Sierra Nevada (light and dark blue) than in the northern basins (purple and red) due to elevational differences (Fig. 13 A and B).

For additional perspective, we consider the most densely sampled elevations across the Sierra Nevada based on the California Department of Water Resources in situ observations (cdec.water.ca.gov/snow/current/snow/index.html). Within this network, the average snow pillow elevation is ~2,300 m and these observations serve as an indicator of the amount of SWE across the range, rather than a direct measure of the SWE volume. Over 60% of the sensor measurements occur below 2,540 m, which is the average elevation of z_c on 1 April (Figs. 13C and 14). Snow courses in the Sierra Nevada have a similar elevational distribution. Thus, on average, about half of the SWE across the range is located at elevations above the majority of the sampling network. Also, not all of the basins in Fig. 13A have observations.

Undersampling the highest elevations with the current in situ network can misrepresent the amount of SWE stored and where its center of mass is located in space and time (Fig. 13C). Although high elevations make up a smaller fraction of the total area than lower elevations (Fig. 13B), they will play an increasingly important role in a warmer climate since warmer temperatures generally melt SWE at lower elevations resulting in a higher snow line and SWE centroid (24). Thus, the northern Sierra Nevada and in particular the NW, with the lowest winter SWE centroid (Fig. 13C), are likely most susceptible to warming. Also, the strongest correlations between winter temperature and both 1 April SWE and z_c occur in the NW. Not only do warmer temperatures shift the partitioning of total precipitation from snowfall toward rainfall, but also snow that occurs at these elevations would likely melt sooner under warmer conditions. While other hydrometeorological drivers beyond temperature (e.g., precipitation) impact SWE, the focus of this study is on understanding SWE distributions conditioned on temperature. In fact, at the highest elevations, a larger proportion of the total precipitation becomes SWE than at lower elevations.

Since water managers typically use the 1 April SWE as a metric for estimating melt-derived runoff, the remainder of this study focuses on probabilistically assessing the vulnerabilities/sensitivities of the 1 April SWE storage (amount and centroid) in relation to the average winter temperature.

Fig. 14 presents the regional climatology and interannual variability of the 1 April SWE volume and centroid and average winter temperature. Strong, statistically significant ($P<0.05$) negative correlations exist between the SWE volume and z_c with the regional correlation coefficients ranging from −0.66 (NW) to −0.80 (SE). A weaker rangewide correlation exists ($r=-0.53$) due to differences among the regions (e.g., elevation) that greatly contrast between the northern and southern Sierra Nevada and degrade its strength relative to the individual regions. Nonetheless, a smaller SWE volume tends to correspond to a higher centroid elevation than when a larger SWE volume occurs.

The peak elevation of a region physically constrains the maximum possible elevation of z_c. As such, it is expected that z_c will often be lower in the northern Sierra Nevada. Warmer temperatures reduce the SWE volume, thereby increasing the height of its centroid (Fig. 14). Stronger correlations exist between temperature and z_c than between temperature and SWE. Approximately 38% (SE) to 69% (NW) of the variance in z_c is explained by temperature variability, whereas temperature only explains ~14% (SE) to 37% (NW) of the variance in SWE. These relationships are consistent with previous research that found strong correlations between the intermittent melt and the accumulated 1 April SWE in the Sierra Nevada. Regional differences in intermittent melt rates/patterns contribute to variability in the strength of the correlations. Using the Theil–Sen trend estimator, a decreasing SWE trend from WY 1985–2015 of ~ −22 km^3 SWE per century is found.

Although 1 April is often taken to represent the end of the accumulation season, the 32-y average day-of-peak SWE across each region occurs earlier (9–16 March) with individual regions yielding extreme early (i.e., 21 December) to late (i.e., 9 May) dates for a given year. Hence, the melt season often begins before April. While our focus is on the accumulation season, other environmental controls impact the SWE distribution and melt rate and their relative importance fluctuates across seasons, mountain ranges, etc.

With the western side of the mountain range facing into the prevailing winds, the NW and SW have larger average SWE volumes (dashed vertical lines in Fig. 14) than the eastern basins in the rain shadow. Corresponding to the higher mean elevation in the eastern basins (relative to the western basins, Fig. 1B), the NE has a higher average centroid than the NW on 1 April (Figs. 13C and 14). The same relationship is observed between the SE and SW. Also, the western Sierra Nevada has greater interannual variability of SWE and centroid values than the eastern regions (Fig. 14). In all regions, the extremely warm 2015 winter was the warmest winter season, which corresponded to the highest SWE centroid in the Sierra Nevada during this record.

However, the coolest winter (WY 1985) neither corresponded to the largest SWE nor lowest z_c in any of the regions.

Fig. 14 (Bottom Right) summarizes the interannual variability of the average winter temperature. Only the NW has a positive long-term average temperature (i.e., 0.6 °C), while the other basins have subzero average temperatures (⟨Ta⟩, "×" symbols), with the lowest occurring in the SW at −0.9 °C. The difference in ⟨Ta⟩ values between the NW and SW is ~1.6 °C, which is 5.4 times larger than the difference between the NE and SE. While the rangewide temperatures span more than 2 °C about its mean value, this is not the case for all of the regions. Therefore, we explore the risk associated with a 1.0–2.0 °C temperature change around the rangewide average air temperature, but only consider a 1.0 °C change for the subregions.

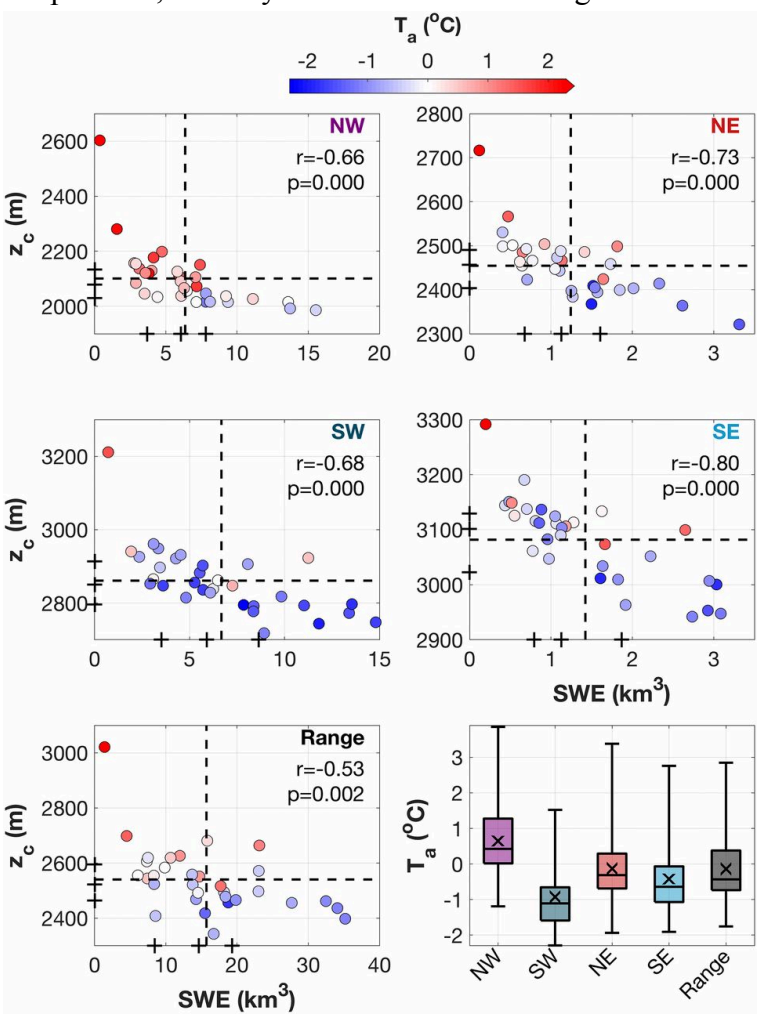

Fig. 14. Scatterplots of annual SWE volume and z_c values on 1 April where the shading of the circles represents the average winter temperature for each of the 32 y. Correlation coefficients (and P values) between the SWE volume and centroid are shown. Plus signs demarcate the 25th, 50th, and 75th quartiles along the respective axes. Dashed lines demarcate the long-term average values. (Bottom Right) Average winter temperature distribution for each region. Whiskers span the range of the data. Long-term averages are indicated with "×" symbols.

Fig. 14 (Top Left) presents the rangewide SWE distribution sampled for various temperatures including ±0.5, ±0.75, and ±1.0 °C about the mean. These temperatures correspond to 1.0, 1.5, and 2.0 °C changes centered on ⟨Ta⟩, respectively. The SWE distributions that are generated for cooler (warmer) temperatures than the 32-y average are blue (red), while the black curve denotes the SWE distribution corresponding to ⟨Ta⟩. The probability density functions (PDFs) become more strongly skewed toward smaller SWE values with increasing temperatures, indicating that less SWE is more probable with warmer temperatures (Fig. 15, Top Left). The likelihood that the long-term average SWE volume (dashed line) will be exceeded decreases with warming as Fig. 15 (Bottom Left) summarizes.

For a 1.0 °C change from 0.5 °C below to 0.5 °C above the mean value, it becomes 20.7% less likely that the SWE volume will be larger than its long-term average value ⟨SWE⟩, which corresponds to exceedance probabilities of 54.3% at −0.6 °C and 33.7% at 0.4 °C. As the temperature change about the mean increases to 1.5 and 2.0 °C, the likelihood of exceeding the average SWE further decreases. For a 1.5 °C increase (from −0.9 to 0.6 °C), it is 31.0% less likely that the long-term SWE will be exceeded, with ~0.6 °C corresponding to an exceedance probability of 30.4%. Similarly for a 2.0 °C change, it is 41.1% less likely that the SWE volume will be larger than ⟨SWE⟩ when the temperature changes from −1.1 °C (Pe=68.4%) to 0.9 °C (Pe=27.3%). Therefore, the change in the exceedance probability for 2.0 °C is ~1.3 and 2.0 times larger than for the 1.5 and 1.0 °C changes, respectively.

We similarly assess the vulnerability of the SWE centroid in Fig. 15 (Right) for the same temperatures. As evident in Fig. 15 (Top Right), the distribution of zc shifts toward higher elevations when warmer winters occur. This shift is consistent with the inverse relationship observed in Fig. 14 between the SWE volume and its centroid, causing the PDFs in Fig. 15 (Top Left) to shift toward lower SWE values and those in Fig. 15 (Top Right) to shift toward higher elevations under warmer conditions. As a result, Fig. 15 (Bottom Right) shows that for the colder than average temperatures considered, the probability that the SWE centroid is lower than its 32-y average value ranges from 98.3% (at ⟨Ta⟩−1.0◦C) to 82.8% (at ⟨Ta⟩−0.5◦C). It drastically decreases to 22.1% at ⟨Ta⟩+0.5◦C and 8.5% at ⟨Ta⟩+1.0◦C for warmer than average temperatures. A temperature 1.0 °C above ⟨Ta⟩ is 5.8% and 13.7% less likely to have a lower than average centroid than when the winter temperature is 0.75 and 0.5 °C above ⟨Ta⟩, respectively. Overall, increases in the winter temperature of 1.0, 1.5, and 2.0 °C about ⟨Ta⟩ result in changes in the nonexceedance probabilities of −60.6%, −79.3%, and −89.8%, respectively (Fig. 15, Right).

Under warmer atmospheric conditions, it is highly probable that the centroid will be forced to higher elevations than its long-term historical location. Also, less of the snowpack will be monitored within the existing in situ network since the centroid will likely reside above the majority of in situ sites, sampling less of the 1 April SWE distribution. Changes in the distribution of montane SWE will present new challenges for monitoring the SWE storage and

forecasting the potential spring/summer runoff. These findings emphasize the importance of generating, maintaining, and improving near-real-time–distributed SWE data.

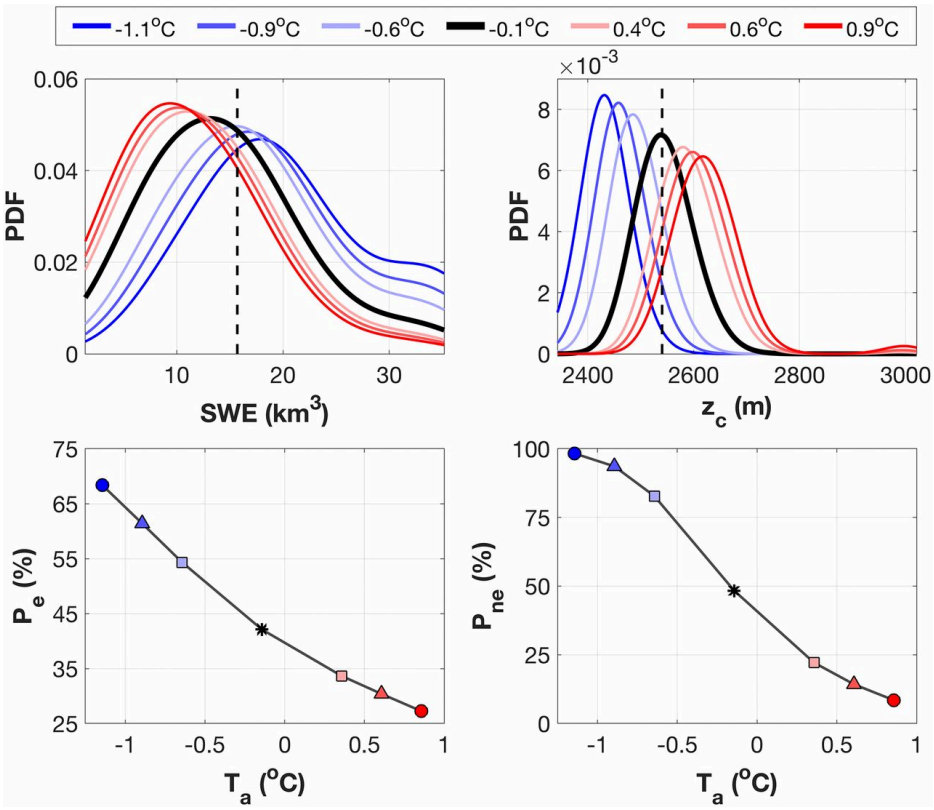

Fig. 15. Impact of 1.0, 1.5, and 2.0 °C of variability about the long-term average winter temperature in the Sierra Nevada. (Top) PDFs for rangewide 1 April SWE (Left) and zc (Right) given select average winter temperatures. Dashed lines demarcate the long-term average SWE and zc values (same as Fig. 14). Limits of x axes are set to the data limits. (Bottom Left) The likelihood that the SWE volume is larger than the long-term average SWE at different temperatures. (Bottom Right) The likelihood that zc is lower than its long-term average given the same temperatures.

Conclusion

As temperatures are projected to rise across California, a key question emerges: To what extent do hydrologic variables respond to different levels of warming? Hence, we characterize the range of historical snowpack responses given 1.0–2.0 °C of warming across the Sierra Nevada. The response is magnified as the amount of warming increases, which is demonstrated by it becoming less likely for the SWE volume (centroid) to be larger (lower) than its long-term average value for a 2.0 °C versus 1.5 or 1.0 °C change about the long-term mean temperature. We show that the change in the likelihood of above average SWE for a 2.0 °C change is twice as large as that for a 1.0 °C change, whereas the change in the likelihood of a lower than average SWE centroid for a 2.0 °C change is ~1.5 times larger than for a 1.0 °C change. Although we do

not use climate projections, results highlight the significance of even small changes in temperature (e.g., 1.5 °C vs. 2.0 °C of warming). Also, point-scale measurements alone cannot yield robust estimates of the montane SWE centroid as done here, which provide valuable information for water managers.

Using a multivariate approach that is adaptable to other SWE characteristics and hydrometeorological forcings, we probabilistically identify water resources vulnerabilities to provide insight into plausible SWE responses to climate change. The northern Sierra Nevada exhibits a greater susceptibility to warming than the southern portion, where the change in the likelihood of above average SWE given 1.0 °C of warming is twice as large in the NW as in the SE. The larger northern response poses risk for increased future wildfire activity given that the region has historically been vulnerable to wildfires with shifts in snowmelt timing. Warmer winters reduce the 1 April SWE and force its centroid to higher elevations above the majority of the in situ network, which can have major implications in water resources management, flood control, hydropower generation, etc. Given the generality of our framework, our model can be applied to other snow-covered mountain ranges across the globe.

Publications since the beginning of the project

Madadgar S., AghaKouchak A., Shukla S., Wood A.W., Cheng L., Hsu K., Svoboda M., 2016, A Hybrid Statistical-Dynamical Drought Prediction Framework: Application to the Southwestern United States, Water Resources Research, doi: 10.1002/2015WR018547.

Chiang F., Mazdiyasni O., AghaKouchak A., 2018, Amplified Warming of Droughts in Southern United States in Observations and Model Simulations, *Science Advances*, 4, doi: 10.1126/sciadv.aat2380.

Huning L., AghaKouchak A., 2018, Mountain Snowpack Response to Different Levels of Warming, *Proceedings of the National Academy of Sciences*, doi: 10.1073/pnas.1805953115.

Mamalakis A., Yu J.-Y., Randerson J.T., AghaKouchak A., Foufoula-Georgiou E., 2018, A New Interhemispheric Teleconnection Increases Predictability of Winter Precipitation in Southwestern US, *Nature Communications*, 9, 2332, doi: 10.1038/s41467-018-04722-7.

AghaKouchak A., Huning L., Chiang F., Sadegh M., Vahedifard F., Mazdiyasni O., Moftakhari H., Mallakpour I., 2018, How do Natural Hazards Cascadeto Cause Disasters?, *Nature*, 561, 458-460 , doi: 10.1038/d41586-018-06783-6.

AghaKouchak A., Cheng L., Mazdiyasni O., Farahmand A., 2014, Global Warming and Changes in Risk of Concurrent Climate Extremes: Insights from the 2014 California Drought, *Geophysical Research Letters*, 41, 8847-8852, doi: 10.1002/2014GL062308.

AghaKouchak A., 2014, A Baseline Probabilistic Drought Forecasting Framework Using Standardized Soil Moisture Index: Application to the 2012 United States Drought, *Hydrology and Earth System Sciences*, 18, 2485-2492, doi: 10.5194/hess-18-2485-2014.

Cheng L., Hoerling M., AghaKouchak A., Livneh B., Quan X.-W., Eischeid J., 2016, How Has Human-induced Climate Change Affected California Drought Risk?, *Journal of Climate*, 29, 111-120, doi: 10.1175/JCLI-D-15-0260.1.

AghaKouchak A., 2015, A Multivariate Approach for Persistence-Based Drought Prediction: Application to the 2010-2011 East Africa Drought, *Journal of Hydrology*, 526, 127-135, doi: 10.1016/j.jhydrol.2014.09.063.

Farahmand A., AghaKouchak A., 2015, A Generalized Framework for Deriving Nonparametric Standardized Drought Indicators, *Advances in Water Resources*, 76, 140-145.

Technical Readiness Level (TRL)

TRL: 5

We have shared the source codes of the Hybrid Statistical-Dynamical model with the California Department of Water Resources (CADWR). We have also shared the source codes for a simpler version of the code and we are expecting feedback later this summer. The CADWR plans to test the model independently. We expect to identify the strength and limitations throughout the process.

References

AghaKouchak, A., Feldman, D., Hoerling, M., Huxman, T., and J. Lund (2015), Recognize Anthropogenic Drought, Nature, 524 (7566), 409-4011, doi:10.1038/524409a.

AghaKouchak, A., Cheng, L., Mazdiyasni, O., and A. Farahmand (2014), Global warming and changes in risk of concurrent climate extremes: Insights from the 2014 California drought, Geophys. Res. Lett., 41, 8847–8852, doi:10.1002/2014GL062308.

Bougeault, P., Toth, Z., Bishop, C., Brown, B.G., Burridge, D., Chen, D., Ebert, B., Fuentes, M., Hamill, T.M., Mylne, K., Nicolau, J., Paccagnella, T., Park, Y.-Y., Parsons, D., Raoult, B., Schuster, D., Silva Dias, P., Swinbank, R., Takeuchi, Y., Tennant, W., Wilson, L., and S. Worley (2010), The THORPEX Interactive Grand Global Ensemble, Bulletin of the American Meteorological Society, 91, 1059-1072.

Becker, E., van den Dool, H., and Q. Zhang (2014), Predictability and Forecast Skill in NMME, J. Climate, 27, 5891–5906.

Bradley, R. S., H. F. Diaz, G. N. Kiladis, and J. K. Eischied (1987), ENSO signal in continental temperature and precipitation records, Nature, 327, 497–501.

Buser, C. M., Künsch, H. R., and C. Schär (2010), Bayesian multi-model projections of climate: Generalization and application to ENSEMBLES results, Climate Res., 44, 227–241.

Cayan, D. R., Dettinger, M. D., Diaz, H. F., and N. E. Graham (1998), Decadal variability of precipitation over western North America, Journal of Climate, 11(12), 3148-3166.

Cayan, D. R., Das, T., Pierce, D. W., Barnett, T. P., Tyree, M., and A. Gershunov (2010), Future dryness in the southwest US and the hydrology of the early 21st century drought, Proc. Natl. Acad. Sci., 107, 21,271–21,276.

Cheng L., and A. AghaKouchak (2015), A Methodology for Deriving Ensemble Response from Multimodel Simulations, Journal of Hydrology, 522, 49-57, doi: 0.1016/j.jhydrol.2014.12.025.

Cheng, L., et al., (2016), How Has Human-induced Climate Change Affected California Drought Risk?, Journal of Climate, 29, 111-120.
Coelho, C. A. S., Pezzulli, S., Balmaseda, M., Doblas-Reyes, F. J., and D. B. Stephenson (2004), Forecast Calibration and Combination: A Simple Bayesian Approach for ENSO, J. Climate, 17, 1504–1516.
Cohen, J., and J. Jones (2011), A new index for more accurate winter predictions, Geophys. Res. Lett. 38, L21701.
Cook, B. I., Ault, T. R., and J. E. Smerdon (2015), Unprecedented 21st century drought risk in the American Southwest and Central Plains, Science Advances,1(1), e1400082.
DeFlorio, M. J., Pierce, D. W., Cayan, D. R., and A. J. Miller (2013), Western U.S. Extreme Precipitation Events and Their Relation to ENSO and PDO in CCSM4, J. Climate, 26, 4231–4243.
Dettinger, M. D. (2013), Atmospheric Rivers as Drought Busters on the U.S. West Coast, J. Hydrometeor, 14, 1721–1732.
Diaz, H. F., and G. N. Kiladis (1992), Atmospheric teleconnections associated with the extreme phase of the Southern Oscillation. El Nino: Historical and Paleoclimatic Aspects of the Southern Oscillation, H. F. Diaz and V. Markgraf, Eds., Cambridge University Press, 7–28.
Dupuis, D. J. (2007), Using Copulas in Hydrology: Benefits, Cautions, and Issues, J. Hydrol. Eng., 12(4), 381-393.
Embrechts, P., Lindskog, F., and A. J. McNeil (2003), Modelling dependence with copulas and applications to risk management, Handbook of heavy tailed distributions in finance, S. T. Rachev, ed., Elsevier Science, Amsterdam, Netherlands.
Favre, A. C., Adlouni, S. E., Perreault, L., Thiéonge, N., and B. Bobée (2004), Multivariate hydrological frequency analysis using copulas, Water Resour. Res., 40(1), W01101.
Folland, C., Owen, J., Ward, M. N., and A. Colman (1991), Prediction of seasonal rainfall in the Sahel region using empirical and dynamical methods, Journal of Forecasting, 10(1, 2), 21.
Gao, H., Wang, Y.G., and J.H. He (2006), Weakening significance of ENSO as a predictor of summer precipitation in China, Geophys. Res. Lett., 33, L09807.
Gershunov, A. (1998), ENSO Influence on Intraseasonal Extreme Rainfall and Temperature Frequencies in the Contiguous United States: Implications for Long-Range Predictability, J. Climate, 11, 3192–3203.
Gimeno, L., Nieto, R., Vázquez, M., and D. A. Lavers (2014), Atmospheric rivers: a mini-review, Frontiers in Earth Science, 2, 2.
Guan, B., Waliser, D. E., Molotch, N. P., Fetzer, E. J., and P. J. Neiman (2012), Does the Madden–Julian Oscillation Influence Wintertime Atmospheric Rivers and Snowpack in the Sierra Nevada?, Mon. Wea. Rev., 140, 325–342.
Guan, B., Molotch, N. P., Waliser, D. E., Fetzer, E. J., and P. J. Neiman (2013), The 2010/2011 snow season in California's Sierra Nevada: Role of atmospheric rivers and modes of large-scale variability, Water Resources Research, 49(10), 6731-6743.
Hao Z., and A. AghaKouchak (2013), Multivariate Standardized Drought Index: A Parametric Multi-Index Model, Advances in Water Resources, 57, 12-18, doi: 10.1016/j.advwatres.2013.03.009.
Harris, I., P. D. Jones, T. J. Osborn, and D. H. Lister (2014) Updated high-resolution grids of monthly climatic observations – the CRU TS3.10 Dataset. Int. J. Climatol., 34, 623-642, doi:10.1002/joc.3711.

Hartmann, H., Becker, S., and L. King (2008), Predicting summer rainfall in the Yangtze River basin with neural networks, Int. J. Climatol., 28, 925–936.
Hewitt, C. D. (2004), Ensembles-based predictions of climate changes and their impacts, Eos, Transactions American Geophysical Union, 85(52), 566-566.
Hoerling, M. P., Kumar, A., and M. Zhong (1997), El Niño, La Niña, and the Nonlinearity of Their Teleconnections, J. Climate, 10, 1769–1786.
Infanti, J. M., and B. P. Kirtman (2015), North American rainfall and temperature prediction response to the diversity of ENSO, Climate Dynamics, 1-17.
Jia, L., Yang, X., Vecchi, G. A., Gudgel, R. G., Delworth, T. L., Rosati, A., Stern, W. F., Wittenberg, A. T., Krishnamurthy, L., Zhang, S., Msadek, R., Kapnick, S., Underwood, S., Zeng, F., Anderson, W. G., Balaji, V., and K. Dixon (2015), Improved Seasonal Prediction of Temperature and Precipitation over Land in a High-Resolution GFDL Climate Model, J. Climate, 28, 2044–2062.
Joe, H. (1997), Multivariate Models and Dependence Concepts, Chapman & Hall, London.
Johnson, C. R. (1970), Positive Definite Matrices, Amer. Math. Monthly 77, 259-264.
Kao, S., and R. S. Govindaraju (2008), Trivariate statistical analysis of extreme rainfall events via Plackett family of copulas, Water Resour Res, 44(2), W02415.
Keeley, J. E., Safford, H., Fotheringham, C. J., Franklin, J., and M. Moritz (2009), The 2007 southern California wildfires: lessons in complexity, Journal of Forestry, 107(6), 287-296.
Kelly, K. S., and R. Krzysztofowicz (1997), A bivariate meta-Gaussian density for use in hydrology, Stochastic Hydrology and Hydraulics, 11(1), 17-31.
Khedun, C. P., Mishra, A. K., Singh, V. P., and J. R. Giardino (2014), A copula-based precipitation forecasting model: Investigating the interdecadal modulation of ENSO's impacts on monthly precipitation, Water Resources Research, 50(1), 580-600.
Kiladis, G. N., and H. F. Diaz (1989), Global climate anomalies associated with extremes of the Southern Oscillation, J. Clim., 2, 1069-1090.
Kim, H. M., Webster, P. J., and J. A. Curry (2012), Seasonal prediction skill of ECMWF System 4 and NCEP CFSv2 retrospective forecast for the Northern Hemisphere Winter, Climate Dynamics, 39(12), 2957-2973.
Kirtman, B. P., Min, D., Infanti, J. M., et al. (2014), The North American Multimodel Ensemble: Phase-1 Seasonal-to-Interannual Prediction; Phase-2 toward Developing Intraseasonal Prediction, Bull. Amer. Meteor. Soc., 95, 585–601.
Knutti, R., Furrer, R., Tebaldi, C., Cermak, J., and G. A. Meehl (2010), Challenges in combining projections from multiple climate models, J. Clim. 23 (10), 2739– 2758.
Krishnamurti, T., Kishtawal, C., Zhang, Z., LaRow, T., Bachiochi, D., Williford, E., Gadgil, S., and S. Surendran (2000), Multimodel ensemble forecasts for weather and seasonal climate. J. Clim. 13 (23), 4196–4216.
Kumar, A., Bhaskar, J., Zhang, Q., and L. Bounoua (2007), A new methodology for estimating the unpredictable component of seasonal atmospheric variability, J. Clim., 20, 3888–3901.
Kurtzman, D., and B. R. Scanlon (2007), El Nino-Southern Oscillation and Pacific Decadal Oscillation impacts on precipitation in the southern and central United States: Evaluation of spatial distribution and predictions, Water Resour. Res., 43, W10427, doi:10.1029/2007WR 005863.
Lavers, D. A., and G. Villarini (2013), The nexus between atmospheric rivers and extreme precipitation across Europe, Geophysical Research Letters, 40(12), 3259-3264.

Luo, L., E. F. Wood, and M. Pan (2007), Bayesian merging of multiple climate model forecasts for seasonal hydrological predictions, J. Geophys. Res., 112, D10102, doi:10.1029/2006JD007655.

Ma, F., Ye, A., Deng, X., Zhou, Z., Liu, X., Duan, Q., Xu, J., Miao, C., Di, Z. and Gong, W. (2015), Evaluating the skill of NMME seasonal precipitation ensemble predictions for 17 hydroclimatic regions in continental China, Int. J. Climatol.. doi: 10.1002/joc.4333.

Madadgar, S., Moradkhani, H. (2013), A Bayesian Framework for Probabilistic Seasonal Drought Forecasting, J. Hydrometeorology (AMS), 14, 1685–1705.

Madadgar, S., Moradkhani, H., and D. Garen (2014), Towards Improved Post-processing of Hydrologic Forecast Ensembles, Hydrological Processes, 28: 104–122.

Madadgar, S., and H. Moradkhani (2015), Improved Bayesian multimodeling: Integration of copulas and Bayesian model averaging, Water Resour. Res., 50, 9586–9603, doi:10.1002/2014WR015965.

Mantua, N. J., Hare, S. R., Zhang, Y., Wallace, J. M., and R. C. Francis (1997), A Pacific interdecadal climate oscillation with impacts on salmon production, Bulletin of the american Meteorological Society, 78(6), 1069-1079.

Masson, D. and R. Knutti (2011), Climate model genealogy, Geophys. Res. Lett. 38, L08703.

Maurer, E. P., L. Brekke, T. Pruitt, and P. B. Duffy (2007), Fine-resolution climate projections enhance regional climate change impact studies, Eos Trans. AGU, 88, 504.

McCabe, G. J., and M. D. Dettinger (1999), Decadal variations in the strength of ENSO teleconnections with precipitation in the western United States, Int. J. Climatol., 19(13), 1399–1410.

McCabe, G. J., Palecki, M. A., and J. L. Betancourt (2004), Pacific and Atlantic Ocean influences on multidecadal drought frequency in the United States, Proceedings of the National Academy of Sciences (PNAS), 101(12), 4136-4141.

Merryfield, W. J., Lee, W. S., Boer, G. J., Kharin, V. V., Scinocca, J. F., Flato, G. M., Ajayamohan, R. S., Fyfe, J. C., Tang, Y., and S. Polavarapu (2013), The Canadian Seasonal to Interannual Prediction System. Part I: Models and Initialization, Mon. Wea. Rev.,141, 2910–2945.

Najafi, M., R., and H. Moradkhani (2015), Ensemble Combination of Seasonal Streamflow Forecasts, J Hydrologic Engineering, 10.1061/(ASCE)HE.1943-5584.0001250, 04015043.

Nelsen, R. B. (1999), An Introduction to Copulas, Springer, New York.

Obled, C., Bontron, G., and R. Garçon (2002), Quantitative precipitation forecasts: a statistical adaptation of model outputs through an analogues sorting approach, Atmospheric research, 63(3), 303-324.

Palmer, T. N. et al. (2004), Development of a European multimodel ensemble system for seasonal-to-interannual prediction (DEMETER), Bulletin of the American Meteorological Society, 85(6), 853-872.

Peng, Z., Wang, Q. J., Bennett, J. C., Pokhrel, P., and Z. Wang (2014), Seasonal precipitation forecasts over China using monthly large-scale oceanic-atmospheric indices, J Hydrology, 519, 792-802.

Raftery, A. E., Gneiting, T., Balabdaoui, F., and M. Polakowski (2005), Using Bayesian Model Averaging to Calibrate Forecast Ensembles, Mon. Wea. Rev., 133, 1155-1174.

Rajeevan, M., Pai, D. S., Kumar, R. A., and B. Lal (2007), New statistical models for long-range forecasting of southwest monsoon rainfall over India, Climate Dynamics, 28(7-8), 813-828.

Ralph, F. M., Neiman, P. J., Kiladis, G. N., Weickmann, K., and D. W. Reynolds (2011), A Multiscale Observational Case Study of a Pacific Atmospheric River Exhibiting Tropical–Extratropical Connections and a Mesoscale Frontal Wave, Mon. Wea. Rev., 139, 1169–1189.

Rasmusson, E. M., and J. M. Wallace (1983), Meteorological aspects of the El Nino/Southern Oscillation, Science, 222, 1195–1202.

Redmond, K. T., and R. W. Koch (1991), Surface climate and streamflow variability in the western United States and their relationship to largescale circulation indexes, Water Resour. Res., 27, 2381-2399.

Ropelewski, C. F., and M. S. Halpert (1986), North American precipitation and temperature patterns associated with the El Nino/Southern Oscillation (ENSO), Mon. Weather Rev., 114(12), 2352–2362.

Saha, S., Moorthi, S., Wu, X., Wang, J., Nadiga, S., Tripp, P., Behringer, D., Hou, Y., Chuang, H., Iredell, M., Ek, M., Meng, J., Yang, R., Peña Mendez, M., van den Dool, H., Zhang, Q., Wang, W., Chen, M., and E. Becker (2014), The NCEP Climate Forecast System Version 2. J. Climate, 27, 2185–2208.

Savtchenko, A. K., Huffman, G., and B. Vollmer (2015), Assessment of precipitation anomalies in California using TRMM and MERRA data, Journal of Geophysical Research: Atmospheres, 120(16), 8206-8215.

Schepen, A., Wang, Q. J., and D. Robertson (2012), Evidence for Using Lagged Climate Indices to Forecast Australian Seasonal Rainfall, J. Climate, 25, 1230–1246.

Schepen, A., and Q. J. Wang (2013), Towards accurate and reliable forecasts of Australian seasonal rainfall by calibrating and merging multiple coupled GCMs, Mon. Weather Rev. 141, 4554–4563.

Schepen, A. Wang, Q. J., and D. E. Robertson (2014), Seasonal Forecasts of Australian Rainfall through Calibration and Bridging of Coupled GCM Outputs, Mon. Wea. Rev., 142, 1758–1770.

Seager, R., Kushnir, Y., Herweijer, C., Naik, N., and J. Velez (2005), Modeling of tropical forcing of persistent droughts and pluvials over western North America: 1856–2000, J. Clim., 18, 4065–4088.

Seager, R., et al. (2007), Model projections of an imminent transition to a more arid climate in southwestern North America, Science, 316(5828), 1181–1184.

Seager, R., Hoerling, M., Schubert, S., Wang, H., Lyon, B., Kumar, A., Nakamura, J. and N. H. Henderson (2014), Causes and predictability of the 2011-14 California Drought: assessment report, NOAA Modeling, Analysis, Predictions and Projections Program (MAPP), National Integrated Drought Information System (NIDIS)

Sharma, A. (2000), Seasonal to interannual rainfall probabilistic forecasts for improved water supply management: Part 3 — A nonparametric probabilistic forecast model, Journal of Hydrology, 239 (1–4): 249–258.

Shukla, S., Steinemann, A., Iacobellis, S. F., and D. R. Cayan (2015), Annual Drought in California: Association with Monthly Precipitation and Climate Phases, Journal of Applied Meteorology and Climatology, (2015).

Shukla, S., et al., (2015), Temperature impacts on the water year 2014 drought in California, Geophys. Res. Lett., 42, 4384–4393.

Tang, Q., Wood, A. W., and D. P. Lettenmaier (2009), Real-Time Precipitation Estimation Based on Index Station Percentiles, J. Hydrometeor, 10, 266–277.

Trenberth, K. E. (1984), Signal versus noise in the Southern Oscillation, Mon. Weather Rev., 112(2), 326-332.
Trenberth, K.E. (1997), The definition of El Nino, Bull. Am. Meteorol. Soc., 78, 2771–2777.
Wang, B., et al (2009), Advance and prospectus of seasonal prediction: assessment of the APCC/CliPAS 14-model ensemble retrospective seasonal prediction (1980–2004), Climate Dynamics, 33(1), 93-117.
Vovk, V. (2001), Competitive on-line statistics, Int. Stat. Rev., 69 (2), 213–248.
Weigel, A. P., M. A. Liniger, and C. Appenzeller (2008), Can multi-model combination really enhance the prediction skill of probabilistic ensemble forecasts?, Q. J. R. Meteorol. Soc., 134, 241–260, doi:10.1002/qj.210.
Weigel, A. P., R. Knutti, M. A. Liniger, and C. Appenzeller (2010), Risks of model weighting in multimodel climate projections, J. Clim., 23, 4175–4191.
Wen, C., Kumar, A., and Y. Xue (2014), Factors contributing to uncertainty in Pacific Decadal Oscillation index, Geophysical Research Letters, 41(22), 7980-7986.
Westerling, A. L., Gershunov, A., Brown, T. J., Cayan, D. R., and M. D. Dettinger (2003), Climate and Wildfire in the Western United States, Bull. Amer. Meteor. Soc., 84, 595–604.
Wood, A. W. (2008, January), The University of Washington Surface Water Monitor: An experimental platform for national hydrologic assessment and prediction, In American Meteorology Society annual meeting, 22nd conference on hydrology, New Orleans. p (Vol. 13).
Woodhouse, C. A., Meko, D. M., MacDonald, G. M., Stahle, D. W., and E. R. Cook (2010), A 1,200-year perspective of 21st century drought in southwestern North America, Proceedings of the National Academy of Sciences, 107(50), 21283-21288.
Wu, Z.W., Wang, B., Li, J.P., and F.F. Jin (2009), An empirical seasonal prediction model of the East Asian summer monsoon using ENSO and NAO, J. Geophys. Res., 114, D18120.
Yang, S., Jiang, Y., Zheng, D., Higgins, R. W., Zhang, Q., Kousky, V. E., and M. Wen (2009), Variations of U.S. Regional Precipitation and Simulations by the NCEP CFS: Focus on the Southwest, J. Climate, 22, 3211–3231.
Yue, S., Ouarda, T. B.M. J., and B. Bobée (2001), A review of bivariate gamma distributions for hydrological application, J. Hydrol., 246(1–4), 1–18.
Zhang, S., Harrison, M. J., Rosati, A., and A. T. Wittenberg (2007), System design and evaluation of coupled ensemble data assimilation for global oceanic climate studies. Mon. Wea. Rev., 135, 3541–3564, doi:10.1175 /MWR3466.1.
Zhu, Y., and R. E. Newell (1998), A Proposed Algorithm for Moisture Fluxes from Atmospheric Rivers, Mon. Wea. Rev., 126, 725–735.
Xia, Y., Mitchell, K., Ek, M., Sheffield, J., Cosgrove, B., Wood, E., Luo, L., Alonge, C., Wei, H., Meng, J. and B. Livneh (2012), Continental-scale water and energy flux analysis and validation for the North American Land Data Assimilation System project phase 2 (NLDAS-2): 1. Intercomparison and application of model products, Journal of Geophysical Research: Atmospheres (1984–2012), 117(D3).